A&A 410, 917–935 (2003)
DOI: 10.1051/0004-6361:20031316

Astronomy & Astrophysics

Radial mixing in protoplanetary accretion disks

V. Models with different element mixtures

M. Wehrstedt and H.-P. Gail

Institut für Theoretische Astrophysik, Universität Heidelberg, Tiergartenstraße 15, 69121 Heidelberg, Germany

Received 17 June 2003 / Accepted 14 August 2003

Abstract. Protoplanetary disks as birth places of planets as well as of their host stars bear different element mixtures owing to the different chemical compositions of the environments where they are born. The chemical composition affects the structure and evolution of the disks, particularly the composition and abundance of the dust. In this work we perform one-zone model calculations of vertically selfgravitating protoplanetary accretion disks with the β-prescription for the viscosity with different element mixtures. The models consider the chemical equilibrium condensation of the most important dust species in the disk as well as annealing of interstellar silicate dust and combustion of carbon dust. Also a new inner boundary condition is introduced which avoids the unphysical decline of the surface density Σ of the frequently adopted no-torque ($\Sigma = 0$) condition. The main result of the model calculations is that with decreasing metallicity the disks become less opaque and hence colder as a consequence of the reduced dust-to-gas ratio. Further we give a rough estimate for the critical value of the metallicity below which the formation of terrestrial planets is inhibited.

Key words. accretion, accretion disks – stars: abundances – solar system: formation – dust, extinction

1. Introduction

The evolution of stars is well known to be strongly dependent on the element mixture, particularly on the value of the metallicity [Fe/H]. The influence of variation of the element mixture on the evolution of protoplanetary disks, however, has not been considered so far. On one hand, the element mixture should affect the composition of the dust which is the main absorber in protoplanetary disks, and therefore should have an impact on the radiative transfer and the hydrodynamic evolution of the disk. On the other hand, the process of formation of large bodies in protoplanetary disks, i.e. comets, asteroids and planets, should depend on the dust-to-gas ratio, hence on the abundance of the dust forming elements.

By means of a statistical investigation of the hitherto detected exoplanets, in a recent work Santos et al. (2003) show that the number of giant gaseous planets decreases with decreasing metallicity of their host stars. Santos et al. (2003) conclude that the dominant process of formation of gaseous planets is core accretion (Pollack et al. 1996) rather than gravitational instability (Boss 2000) since the mass of the solid core is reduced with decreasing metallicity and therefore gas accretion onto the core is inhibited below a critical value of [Fe/H]. The authors do not exclude, however, the gravitational instability scenario for the formation of giant planets which could act in massive disks.

Send offprint requests to: M. Wehrstedt,
e-mail: mwehrste@ita.uni-heidelberg.de

With respect to the terrestrial planets it is unclear up to now how their formation is influenced by the metallicity and the details of the element mixture.

In this work we calculate models of vertically selfgravitating protoplanetary accretion β-disks in the one-zone approximation with different element mixtures. Particularly we investigate the modification of the structure and evolution of the disks as well as the modification of the composition of the dust in the disk with decreasing metallicity. The one zone disk model is valid in the early phase of disk evolution, within which large bodies have not yet formed which open gaps in the disk. The condensation and vaporization of the most important dust species in chemical equilibrium with the gas phase in the inner, chemical active disk region is considered. Annealing of silicate grains, combustion of carbon grains and radial mixing of either crystalline silicate and carbon grains are taken into consideration, as Gail (2001) and Wehrstedt & Gail (2002) have shown that these processes are important for the thermal structure of protoplanetary disks. Also vertical selfgravitation of the disk is included in the model calculations. Furthermore we apply a new type of inner boundary condition in the model calculation that we call the "quasistationary" boundary condition. This avoids the unphysical decline of the surface density Σ and unrealistically low temperatures in the innermost disk regions which result from the usually adopted no-torque ($\Sigma = 0$) condition.

The present work is a further contribution within this series which examines the structure and evolution of protoplanetary

disks with particular emphasis on the composition of the dust which, amongst other processes, is strongly affected by mixing processes within the disk. Gail (2001; henceforth Paper I) performed calculations of stationary disk models including radial mixing. These models have been extended to time dependent disk models with radial mixing by Wehrstedt & Gail (2002; henceforth Paper II). Gail (2002; henceforth Paper III) investigated the composition and mixing of the products of carbon combustion, such as methane. Finally, Gail (2003; henceforth Paper IV) in detail calculates the composition of the silicate dust complex. The aim of this series is to determine the composition of planetary system bodies, in particular the composition of the most pristine bodies in our own solar system, the asteroids and comets.

The paper is organized as follows: in Sect. 2 the treatment of equilibrium condensation of the different dust species considered in the model calculations is presented. Section 3 shows how radial mixing is included in the model calculations. The set of equations for the radial disk structure is presented in Sect. 4. Section 5 describes the numerical treatment of the model. The results are shown and discussed in Sect. 6. We summarize the results in Sect. 7 and make our final conclusions in Sect. 8.

2. Condensation of dust species

2.1. Forsterite and enstatite

In Papers I and II forsterite (Mg_2SiO_4) has been assumed to be the only silicate compound in the dust mixture. Here we extend the chemistry of our model and include the condensation of enstatite ($MgSiO_3$) which is treated simultaneously with the condensation of forsterite in chemical equilibrium.

The method of calculating the degrees of condensation of Si into forsterite and enstatite, $f_{\rm for}$ and $f_{\rm ens}$, is as follows:

First the abundances of C and O in the gas phase are calculated from

$$\epsilon_{\rm C,gas} = \epsilon_{\rm C}\,(1 - f_{\rm car})\,, \tag{1}$$

$$\epsilon_{\rm O,gas} = \epsilon_{\rm O} - \epsilon_{\rm C,gas} - (4\,f_{\rm for} + 3\,f_{\rm ens})\,\epsilon_{\rm Si} - \frac{3}{2}\epsilon_{\rm Al}\,f_{\rm cor}. \tag{2}$$

ϵ_X is the abundance of element X. $f_{\rm car}$ and $f_{\rm cor}$ are the degrees of condensation of carbon into solid carbon grains and of aluminum into corundum (Al_2O_3), respectively, where $f_{\rm car}$ is calculated according to Eq. (35) of Paper II. It is assumed that all the carbon in the gas phase is locked into CO, though there might exist a significant fraction of CH_4 and CO_2 in disks at intermediate distance from the protostar (Finocchi et al. 1997; Paper III).

Next the partial pressure of free oxygen atoms $p_{\rm O}$ is

$$x_{\rm O}\,p_{\rm O} = \epsilon_{\rm O,gas} P_{\rm H}. \tag{3}$$

$P_{\rm H}$ is the fictitious pressure of H nuclei if all H is present as free neutral atoms in the gas phase, and $x_{\rm O}$ is given by

$$\begin{aligned} x_{\rm O} = 1 &+ p_{\rm H}\left[K_{\rm p}({\rm OH}) + p_{\rm H} K_{\rm p}({\rm H_2O})\right] \\ &+ p_{\rm Si} K_{\rm p}({\rm SiO}) + p_{\rm Al}\left[p_{\rm H}\left(K_{\rm p}({\rm AlOH})\right.\right. \\ &\left.\left. + p_{\rm O} K_{\rm p}({\rm AlO_2H})\right) + p_{\rm Al} K_{\rm p}({\rm Al_2O})\right], \end{aligned} \tag{4}$$

where $K_{\rm p}(Y)$ is the mass action constant of molecule Y and p_X the partial pressure of free atoms of element X. $P_{\rm H}$ and $p_{\rm H}$ are calculated by Eqs. (54) and (55) of Paper I. The factors x_X are calculated by taking into account all abundant gas phase species in which the element X is bound. For Si and Mg one has

$$x_{\rm Si} = 1 + p_{\rm O} K_{\rm p}({\rm SiO}), \tag{5}$$

if the small fraction of SiS which exists in chemical equilibrium is neglected, and

$$x_{\rm Mg} = 1 \tag{6}$$

since Mg does not form abundant molecular species at elevated temperatures where Mg is not completely bound in solids.

For determining the mole fractions of the solids in a gas-solid mixture their activity is the crucial quantity (e.g. Philpotts 1990). The activities of forsterite and enstatite in the mixture are

$$a_{\rm for} = p_{\rm Si}\,p_{\rm Mg}^2\,p_{\rm O}^4\,{\rm e}^{-\Delta G({\rm for})/RT}, \tag{7}$$

$$a_{\rm ens} = p_{\rm Si}\,p_{\rm Mg}\,p_{\rm O}^3\,{\rm e}^{-\Delta G({\rm ens})/RT}, \tag{8}$$

where R is the gas constant, T the temperature and $\Delta G(Z)$ the free enthalpy of formation of solid Z from free atoms. The values of $K_{\rm p}(Y)$ and $\Delta G(Z)$ are calculated by using data from Sharp & Huebner (1990). In chemical equilibrium of a solid Z with the gas phase the condition $a_Z = 1$ has to be satisfied. By means of this condition the partial pressures $p_{\rm Si}$ and $p_{\rm Mg}$ are specified by Eqs. (7) and (8) while $p_{\rm O}$ is determined by Eq. (3).

With given $p_{\rm Si}$ and $p_{\rm Mg}$ we calculate the degrees of condensation of Si into forsterite and enstatite $f_{\rm for}$ and $f_{\rm ens}$ from the two stoichiometric conditions

$$(1 - f_{\rm for} - f_{\rm ens})\,\epsilon_{\rm Si} P_{\rm H} = x_{\rm Si}\,p_{\rm Si}, \tag{9}$$

$$\epsilon_{\rm Mg} P_{\rm H} - (2\,f_{\rm for} + f_{\rm ens})\,\epsilon_{\rm Si} P_{\rm H} = x_{\rm Mg}\,p_{\rm Mg}. \tag{10}$$

Equations (9) and (10) are the conditions of element conservation for Si and Mg, respectively. Since forsterite is more stable than enstatite under the conditions of protoplanetary disks there exists a temperature region where forsterite exists, but no enstatite. This shows up in the solution of Eqs. (9) and (10) by a negative $f_{\rm ens}$. Thus we have to check whether $f_{\rm ens} < 0$.

If this is not the case, Eqs. (9) and (10) yield the correct values for $f_{\rm for}$ and $f_{\rm ens}$.

If this is true, however, we have to recalculate $p_{\rm Si}$, $p_{\rm Mg}$ and $f_{\rm for}$ from Eqs. (7), (9) and (10) by letting $f_{\rm ens} = 0$ and $a_{\rm for} = 1$, i.e. we have

$$p_{\rm Si} = \frac{{\rm e}^{\Delta G({\rm for})/RT}}{p_{\rm Mg}^2\,p_{\rm O}^4}, \tag{11}$$

$$f_{\rm for} = 1 - \frac{x_{\rm Si}\,p_{\rm Si}}{\epsilon_{\rm Si} P_{\rm H}}, \tag{12}$$

$$p_{\rm Mg} = \left(\epsilon_{\rm Mg} - 2\,f_{\rm for}\epsilon_{\rm Si}\right) P_{\rm H}. \tag{13}$$

Equations (11)–(13) yield a cubic equation for $f_{\rm for}$ which is solved with the Newton-Raphson method up to an accuracy of 10^{-9} for $p_{\rm Mg}$.

If the solution in this case yields $f_{\rm for} < 0$, then silicates do not exist at all ($f_{\rm ens} = f_{\rm for} = 0$) and all Si and Mg is present as gas phase species only, in which case we have:

$$p_{\rm Si} = \frac{\epsilon_{\rm Si} P_{\rm H}}{x_{\rm Si}}, \tag{14}$$

$$p_{\rm Mg} = \frac{\epsilon_{\rm Mg} P_{\rm H}}{x_{\rm Mg}}\cdot \tag{15}$$

In case of $\epsilon_{\rm Si} > \epsilon_{\rm Mg}$ (non-solar abundances) $f_{\rm for}$ and $f_{\rm ens}$ again are calculated from Eqs. (9) and (10), but then one has to check if $f_{\rm for} < 0$. If this is the case it follows $f_{\rm for} = 0$ and all silicon is bound in enstatite, and the excess of Si over Mg is bound in quartz.

2.2. Corundum

We calculate the degree of condensation of corundum $f_{\rm cor}$ and the partial pressure of free Al atoms, $p_{\rm Al}$, from the set of equations (cf. Eqs. (63) and (64) of Paper I)

$$x_{\rm Al} = 1 + p_{\rm H}\Big[K_{\rm p}({\rm AlH}) + p_{\rm O}\Big(K_{\rm p}({\rm AlOH}) + p_{\rm O} K_{\rm p}({\rm AlO_2H})\Big)\Big] + 2 p_{\rm Al} p_{\rm O} K_{\rm p}({\rm Al_2O}), \tag{16}$$

$$(1 - f_{\rm cor})\,\epsilon_{\rm Al} P_{\rm H} = x_{\rm Al} p_{\rm Al}, \tag{17}$$

$$a_{\rm cor} = p_{\rm Al}^2 p_{\rm O}^3 {\rm e}^{-\Delta G({\rm cor})/RT}. \tag{18}$$

with the condition $a_{\rm cor} = 1$ for chemical equilibrium.

2.3. Solution of the equations of dust condensation

Equations (1)–(18) define a non-linear set of equations for the degrees of condensation $f_{\rm for}$, $f_{\rm ens}$ and $f_{\rm cor}$, and the partial pressures of the free atoms of the elements. They are solved by a fixpoint iteration with an accuracy of 10^{-8}.

2.4. Other dust species

Besides forsterite, enstatite and corundum also solid iron, solid carbon, and water ice mantles around dust cores are considered in the model calculation since these species also are important absorbers in protoplanetary disks.

Iron and water ice are assumed to evaporate/condense in chemical equilibrium like forsterite, enstatite and corundum while solid carbon combusts by surface reactions with OH molecules. The treatment of solid iron, water ice and solid carbon in the model calculation is described in Papers I and II.

Astronomical silicates contain besides Mg also a certain fraction of Fe, i.e. they have compositions $\rm Mg_{2x}Fe_{2(1-x)}SiO_4$ (olivine) and $\rm Mg_xFe_{1-x}SiO_3$ (pyroxene) with $0 \le x \le 1$. The consideration of these solid solutions will be the subject of future investigations. Also quartz, considered by Pollack et al. (1994) as a possible mayor dust component in accretion disks, is not considered in this work since the existence of this component is questionable (but see Honda 2003).

3. Radial mixing

3.1. Annealing of silicate

In Papers I and II we showed that thermal annealing of amorphous silicates and radial mixing are important processes in protoplanetary disks. On one hand diffusive mixing of annealed silicates to the outer parts of protoplanetary disks is a natural explanation of the considerable abundance of crystalline silicate in comets (e.g. Hanner et al. 1994; Wooden et al. 1999, 2000; Harker et al. 2002). On the other hand the radial structure of the disk is modified by annealing of silicates due to the an order of magnitude lower opacity of crystalline silicates compared to amorphous silicates.

We consider annealing of forsterite as well as of enstatite in our model calculation. The method is described in Paper I. For the activation energy $E_{\rm a}$ for rearrangement processes in the lattice in the annealing process we choose the values of Fabian et al. (2000), $E_{\rm a}/k_{\rm B} = 39\,100\,{\rm K}$ for forsterite and $E_{\rm a}/k_{\rm B} = 42\,040\,{\rm K}$ for enstatite, respectively.

3.2. Carbon combustion

In protoplanetary disks solid carbon is destroyed by surface reaction with OH molecules (Duschl et al. 1996; Finocchi et al. 1997). This is because combustion of carbon commences at lower temperatures in protoplanetary disks as compared to thermal evaporation. Hence, with increasing temperature carbon grains are completely burnt by reaction with OH before thermal evaporation starts to operate. The carbon combustion is calculated as in Paper II. Note that methane and further aliphatic hydrocarbons are formed due to reactions with the products of the carbon combustion (Finocchi et al. 1997; Paper III). By radial mixing these products are transported outwards within the solar nebula to the location of the formation of comets. Hence carbon combustion combined with radial mixing may explain the large abundance of methane in comets (cf. Paper III).

3.3. The set of diffusion-transport-reaction equations

As described in detail in Paper II we solve a set of diffusion-transport-reaction equations (e.g. Hirschfelder et al. 1964)

$$\frac{\partial c_{i,j}}{\partial t} + v_{\rm r}\frac{\partial c_{i,j}}{\partial r} = \frac{1}{rn}\frac{\partial}{\partial r} rn D_{\rm dg}\frac{\partial c_{i,j}}{\partial r} + \frac{c_{i-1,j}}{\tau_{i-1,i,j}} - \frac{c_{i,j}}{\tau_{i,i+1,j}}\cdot \tag{19}$$

r is the radial distance from the protostar, $v_{\rm r}$ the radial component of the velocity of a tracer, n the total particle density, and $D_{\rm dg}$ the binary diffusion coefficient of a dust tracer of low particle density in the carrier gas, respectively. The binary diffusion coefficient is set to be equal to the viscosity, $D_{\rm dg} = \nu$ (for details see Paper I), i.e. the motion of tracers (micron-sized dust grains) is assumed to be strongly coupled to the gas flow.

Equation (19) describes the time-dependent evolution of the concentration $c_{i,j}$ of a species j which occurs in different modifications i within the flow of the disk. The flow is assumed to be a superposition of an advective part which reflects the accretion flow of the disk, and of a turbulent component which locally acts by diffusional mixing which tends to smooth out any spatial gradient of the concentration $c_{i,j}$.

The species (index j) considered in the present work are solid carbon, forsterite and enstatite, respectively. Carbon grains are assumed to be present in a size spectrum a_i between $a_1 = 0.25\,\mu$m and $a_N = 0.001\,\mu$m, $i = 1 \ldots N$. Forsterite and enstatite grains occur in a sequence of different degrees of crystallization $x_{i,\mathrm{cry}} = 0 \ldots 1$ where $i = 1 \ldots M$.

The dust species are subject of (i) combustion of the carbon grains, i.e. the size of the grains decreases, and (ii) of annealing of the silicate grains, i.e. the degrees of crystallinity of the silicate grains increases. In either case the reactions are unidirectionally. The atomic carbon released into the gas phase is locked up by CO, and will not form solid carbon again. Silicates can not become less crystallized since there exists no process in the disk which could do this. The only likely process for this would be irradiation with energetic (several keV) ions (Demyk et al. 2001) which do not exist in protoplanetary disks. Thus carbon grains only can shrink in size until they disappear and silicate grains only can get more crystallized until their degree of crystallinity is unity. The characteristic timescales of the considered reactions $\tau_{i,i+1,j}$ (last two terms on the r.h.s. of Eq. (19)) are given in Paper II.

The size grid of carbon grains in our computation is spaced logarithmically equidistant, getting more dense to smaller radii of the carbon grains, with $N = 31$ grid points, chosen as in Paper II. For the degree of crystallinity of silicates we choose an equidistant grid with $M = 3$ which is more coarse as compared to Paper II ($M = 11$). We found that this coarser grid does not influence the results of our model calculations. Hence, silicates (forsterite and enstatite) in our model calculations occur as completely amorphous, partially crystalline ($x_{2,\mathrm{cry}} = 0.5$) and completely crystalline grains.

The numerical treatment of the set of Eqs. (19) is fully implicit, as described in Paper II.

4. Radial disk structure

4.1. Selfgravitation of the disk

Observations reveal that protoplanetary disks in classical T Tauri systems have masses up to a few tenths of the central star (see e.g. the review of Natta 1999). Duschl et al. (2000) show for disks with masses larger than $\sim 1/100\,M_*$ the selfgravity of the disk to become important for the disk structure. If the disk mass is not too large (smaller than $\sim 1\,M_*$) the vertical component of the gravitational field of the disk at the disk's surface well approximates the actual gravitational field of the disk. As in terms of Duschl et al. (2000) we call the disk in this case to be "vertical selfgravitating", or "Keplerian selfgravitating", since the orbital (Keplerian) motion close to the midplane of the geometrically thin disk is not influenced by the gravitational potential of the disk. Disks with masses above $\sim 1\,M_*$ are "fully selfgravitating", i.e. the Poisson equation for the star-disk system has to be solved.

Consequently, since we like to model disks with masses up to a few tenths of the stellar mass, we introduce vertical selfgravity of the disk in our model. Then, the equation for the vertical pressure gradient reads

$$\frac{1}{\rho}\frac{\mathrm{d}P}{\mathrm{d}z} = -\frac{GM_*}{r^3}\,z - 4\pi G\sigma, \tag{20}$$

where $\sigma = \int_0^\infty \rho \mathrm{d}z$. The first and the second term on the r.h.s. of Eq. (20) are the vertical components of the gravitational acceleration vector of the star and the disk (Paczyński 1978), respectively. By assuming vertical isothermicity Eq. (20) is easily integrated. The solution yields a quadratic expression for the scale height of the disk which we define as the height where the pressure is reduced to $1/\sqrt{e}$ of the midplane value. The positive solution of this quadratic equation is given by Eq. (25). In case of negligible selfgravity of the disk, i.e. if the second term on the r.h.s. of Eq. (20) vanishes, Eq. (25) reduces to $h_\mathrm{s} = c_\mathrm{s}/\Omega$ which is the well-known expression for the scale height in a non-selfgravitating disk, as used in Papers I and II.

4.2. Viscosity prescription

As selfgravity is introduced in our model the α-prescription for the viscosity (Papers I and II) no longer can be applied. The reason for this is that in regions of the disk where the disk's selfgravity dominates over the star's gravity the disk becomes radially isothermal (Duschl et al. 2000). Since this is unphysically we introduce the β-prescription of the viscosity (Duschl et al. 2000; Huré et al. 2001) in Eq. (23). In case of the β-ansatz the viscosity decouples from the thermodynamics of the disk, and an unphysical radial isothermicity of the disk is avoided. For details of the β-viscosity, see Duschl et al. (2000) and Huré et al. (2001). Note that β essentially is the reciprocal of the critical Reynolds number of the flow.

4.3. Disk equations

The set of equations for the calculation of the radial disk structure of selfgravitating β-disks in the one-zone approximation is (cf. Paper II for non-selfgravitating α-disks):

1) Time evolution of the surface density:

$$\frac{\partial\Sigma}{\partial t} = \frac{3}{r}\frac{\partial}{\partial r}\sqrt{r}\frac{\partial}{\partial r}\nu\Sigma\sqrt{r}. \tag{21}$$

2) Keplerian angular velocity:

$$\Omega = \sqrt{\frac{GM_*}{r^3}}. \tag{22}$$

3) Viscosity:

$$\nu = \beta r^2\Omega. \tag{23}$$

4) Isothermal sound speed:

$$c_\mathrm{s} = \sqrt{\frac{k_\mathrm{B}T_\mathrm{c}}{\mu m_\mathrm{H}}}. \tag{24}$$

5) Pressure scale height:

$$h_\mathrm{s} = \frac{2\pi G\Sigma}{\Omega^2}\left[\sqrt{1+\left(\frac{c_\mathrm{s}\Omega}{2\pi G\Sigma}\right)^2} - 1\right]. \tag{25}$$

6) Mean vertical mass density:

$$\rho_{\rm m} = \frac{\Sigma}{2h_{\rm s}}. \tag{26}$$

7) Mean molecular weight:

$$\mu = \frac{\rho_{\rm m} k_{\rm B} T_{\rm c}}{m_{\rm H}(p_{\rm H} + p_{\rm H_2} + p_{\rm He})}. \tag{27}$$

8) Rosseland and Planck mean of the mass extinction coefficient:

$$\kappa_{\rm R/P} = \kappa_{\rm R/P}(\rho_{\rm m}, T_{\rm c}). \tag{28}$$

9) Rosseland and Planck vertical optical depth:

$$\tau_{\rm R/P} = \frac{1}{2}\Sigma\kappa_{\rm R/P}. \tag{29}$$

10) Viscous dissipation rate:

$$\dot{E}_\nu = \frac{9}{8}\Omega^2\nu\Sigma. \tag{30}$$

11) Effective temperature of the disk surface:

$$\sigma T_{\rm eff}^4 = \left(1 + \frac{1}{4\tau_{\rm P}}\right)\dot{E}_\nu + \sigma T_{\rm cloud}^4. \tag{31}$$

12) Temperature at the midplane:

$$\sigma T_{\rm c}^4 = \left(\frac{3}{4}\tau_{\rm R} + \frac{1}{4\tau_{\rm P}}\right)\dot{E}_\nu + \sigma T_{\rm cloud}^4. \tag{32}$$

4.4. Opacity

The Rosseland mean of the opacity of the silicates is calculated by

$$\kappa_{\rm R,for} = f_{\rm cry,for}\kappa_{\rm R,for,cry} + (1 - f_{\rm cry,for})\kappa_{\rm R,sil,am}, \tag{33}$$

$$\kappa_{\rm R,ens} = f_{\rm cry,ens}\kappa_{\rm R,ens,cry} + (1 - f_{\rm cry,ens})\kappa_{\rm R,sil,am}. \tag{34}$$

Here $\kappa_{\rm R,for,cry}$, $\kappa_{\rm R,ens,cry}$ and $\kappa_{\rm R,sil,am}$ are the Rosseland opacities of crystalline forsterite, crystalline enstatite and amorphous silicate, respectively, each calculated for solar system abundances. No difference is made between amorphous forsterite and amorphous enstatite since in the outer parts of the disk the solid component of the disk material is present as unequilibrated ISM dust (Paper IV).

$f_{\rm cry,for}$ and $f_{\rm cry,ens}$ are the degrees of crystallinity of forsterite and enstatite, respectively. They are derived from the solution of the set of diffusion-transport-reaction Eqs. (19) for silicate annealing (see Eq. (37) of Paper II).

The Rosseland mean of the dust mixture is approximated by the sum of the contributions of the individual dust components,

$$\begin{aligned}\kappa_{\rm R,dust} &= \zeta_{\rm Si}(f_{\rm for}\kappa_{\rm R,for} + f_{\rm ens}\kappa_{\rm R,ens}) + \zeta_{\rm C} f_{\rm car}\kappa_{\rm R,car} \\ &\quad + \zeta_{\rm Fe} f_{\rm iro}\kappa_{\rm R,iro} + \zeta_{\rm Al} f_{\rm cor}\kappa_{\rm R,cor}.\end{aligned} \tag{35}$$

$\kappa_{\rm R,car}$, $\kappa_{\rm R,iro}$ and $\kappa_{\rm R,cor}$ denote the Rosseland opacities of solid carbon, solid iron and corundum, respectively, each calculated for solar system abundances. The f_j are the degrees of condensation of the key dust forming element into the condensate j, i.e. Si for the silicates, C for solid carbon, Fe for solid iron and Al for corundum, respectively. Finally, ζ_X is the ratio of the abundance ϵ_X of element X relative to the solar abundance of this element, $\epsilon_{X,\odot}$, i.e.

$$\zeta_X = \frac{\epsilon_X}{\epsilon_{X,\odot}}. \tag{36}$$

We include the relative abundances ζ_X in the calculation of the opacity since one purpose of the present paper is to calculate models of protoplanetary disks with different metallicities. In Eq. (35) the opacity of each absorber j is multiplied by ζ_X of the key dust forming element of the absorber, as in the case of the f_j, since the opacity κ of a dust species is proportional to the element abundance of the least abundant element required for its formation (the key element).

The degree of condensation of carbon $f_{\rm car}$ is determined by the solution of the set of diffusion-transport-reaction Eqs. (19) for carbon combustion (see Eq. (35) of Paper II).

The Rosseland mean opacity of the gas component is calculated by

$$\kappa_{\rm gas} = \kappa_{\rm H,H_2} + \zeta_{\rm O}\left[\kappa_{\rm OH} + \kappa_{\rm H_2O}\right] + \zeta_{\rm C}\kappa_{\rm CO}, \tag{37}$$

where $\kappa_{\rm H,H_2}$, $\kappa_{\rm OH}$, $\kappa_{\rm H_2O}$ and $\kappa_{\rm CO}$ are the Rosseland mean opacities of hydrogen (atomic and molecular), OH molecules, water vapour and carbon monoxide, respectively. ζ_X is, again, the relative abundance of element X compared to the solar abundance. The κ_j of the gas compounds are calculated from an approximation of Keeley (1979) with the corrections by Marigo (2002). We ignore the contributions of electrons and ions to the opacity as the disks in our model do not become hotter than ∼3000 K at the inner boundary.

The particle densities of the molecular compounds which are needed for the calculation of the opacity according to the fit formula of Keeley (1979) are derived under the assumption of thermodynamical equilibrium by using thermodynamical data of Sharp & Huebner (1990). Dissociation of H_2 is included in the chemical model.

Finally, the Rosseland mean of the opacity of the disk material is calculated by

$$\kappa_{\rm R} = f_{\rm ice}\zeta_{\rm O}\kappa_{\rm R,ice} + (1 - f_{\rm ice})\kappa_{\rm R,dust} + (1 - f_{\rm cor})\kappa_{\rm gas}. \tag{38}$$

Here $f_{\rm ice}$ and $\kappa_{\rm R,ice}$ are the degree of condensation of ice and the Rosseland mean opacity of ice coated grains, respectively, which are calculated as in Paper II. The terms in brackets in Eq. (38) serve for a smooth transition between the opacity of ice coated and bare grains as well as for a smooth transition between the opacity of corundum dust and the opacity of the dust free region. We note that the method for calculating the opacity (sum of the individual absorbers) is exact only in case of a grey atmosphere or in temperature regions where one absorber strongly dominates the opacity.

Disks of low metallicity (small values of ζ_X) clearly have a lower opacity of the disk material. Thus, in disks of low metallicity as compared to disks of solar metallicity, the regions where the vertical optical depth is smaller than unity are

not limited to the outermost disk regions, as for solar metallicity, but will extend much farther inwards. This requires to use in such regions the Planck mean opacities of the individual absorbers j, $\kappa_{\mathrm{P},j}$. The total Planck mean opacity κ_{P} of the dust mixture is calculated in the same way as the total Rosseland mean opacity κ_{R} in Eqs. (33)–(38). From the total Rosseland and Planck mean opacities $\kappa_{\mathrm{R/P}}$ we derive Rosseland and Planck vertical optical depths from Eqs. (29).

The equations for the temperature at the disk surface T_{eff} and at the disk midplane T_{c} of Paper II are replaced by the equations for T_{eff} and T_{c} of Nakamoto & Nakagawa (1994) (Eqs. (31) and (32), respectively) in order to consider correctly also optically thin disk regions. The factors in brackets in Eqs. (31) and (32) serve for a smooth transition between the optically thick and optically thin parts of the disk. In the optical thick case the vertical temperature stratification essentially is an atmosphere in the Eddington approximation.

By using Mie theory and assuming MRN size distributions (Mathis et al. 1977) we calculate κ_λ and from this Rosseland and Planck mean opacities $\kappa_{\mathrm{R/P},j}$ of the individual dust species j. Optical data for amorphous silicate and solid carbon are taken from Draine (1985), for crystalline silicates from the database of the Astrophysical Institut of the University of Jena[1], for solid iron from Lide (1995) and for corundum from Koike et al. (1995), respectively. For calculational purposes κ_{R} and κ_{P} for each dust component are approximated by analytical fit formulas.

In case of ice coated grains we apply the simple T^2 dependence of the Rosseland mean opacity of Bell & Lin (1994) and calculate the Planck mean opacity by using $\kappa_{\mathrm{P,ice}}/\kappa_{\mathrm{R,ice}} = 2.39$ for the ratio between the Planck and Rosseland opacities (Nakamoto & Nakagawa 1994).

We note that the opacity of the disk matter essentially determines the thermal structure of the disk (cf. Papers I and II). With decreasing metallicity, i.e. decreasing ζ_X in (36), the opacity of the disk matter decreases. This especially is important for the dust opacities $\kappa_{\mathrm{R/P,dust}}$ since dust grains are the main absorbers throughout protoplanetary disks, except in their small hot innermost region.

An important process strongly modifying the opacity of the disk material is dust coagulation. This process is neglected in the present calculations. This limits the validity of the present calculations to the period of time until grains form grain cluster of such a size that the approximation of small grains for calculating dust opacity breaks down. In the limit of small grains the opacity essentially depends on the total volume of the condensed material and only marginally on the shape and size of the condensed particles/clusters of condensed material. Assuming a disk temperature of 600 K at 1 AU (corresponding to an evolutionary time of about 5×10^5 yr) Wiens law leads to a wavelength of 4.5 μm for the wavelength of maximum radiative energy flux. If dust grains form cluster of about this size by coagulation, the opacity starts to depend on the degree of coagulation of dust grains. For typical interstellar dust grains of 0.1 μm about 10^5 grains are required for forming clusters of this size.

[1] See: http://www.astro.uni-jena.de

The collision time scale for grain-grain collisions is

$$\tau_{\mathrm{gg}} = \frac{1}{n_{\mathrm{g}} v \sigma}, \tag{39}$$

where n_{g} is the grain particle density, v is the relative velocity between grains, and σ the collision cross section. Typically one has about 10^{-12} ISM grains per hydrogen nucleus, a number density of hydrogen $n_{\mathrm{H}} = 10^{14}\,\mathrm{cm}^{-3}$ at 1 AU, and collision cross sections of $3 \times 10^{-10}\,\mathrm{cm}^2$. For micron-sized particles the relative velocities of particles are determined by Brownian motions which are of the order of 0.1 cm/s (e.g. Weidenschilling & Cuzzi 1993). The typical period of time after which coagulation of dust grains becomes important for the opacity of the dust-gas mixture is of the order of 5×10^5 yr. For lower metallicities this time limit roughly scales as $1/Z$. Thus, coagulation is not important for the opacity calculation except for the very last phases of our solar metallicity model (see Sect. 5.3).

5. Numerical treatment

5.1. Initial and boundary conditions

The initial condition essential is chosen as in Paper II by numerically calculating a stationary model (i.e. $\partial\Sigma/\partial t = 0$ in Eq. (21) and $\partial c_{i,j}/\partial t = 0$ in Eq. (19)) to get an initial radial distribution of the surface density Σ and of the concentrations of carbon grains of different size $c_{i,\mathrm{car}}$. The initial concentrations of forsterite and enstatite grains of different degrees of crystallinity $c_{i,\mathrm{for}}$ and $c_{i,\mathrm{ens}}$ are chosen such that the silicate grains are completely amorphous at the beginning of the integration, i.e. the silicates are assumed to be unaltered ISM grains.

The initial stationary disk model is calculated for prescribed values of the initial disk mass M_{disk} and disk angular momentum J_{disk} (see Sect. 4.2 in Paper II, particularly the radial dependence of the mass accretion rate $\dot{M}(r)$ within the initial model). M_{disk} and J_{disk} are free parameters. The particular values chosen in the model calculations are shown in Table 2.

The boundary conditions for the concentrations $c_{i,j}$ are chosen as follows: the silicates are completely amorphous at the outer boundary and completely crystalline at the inner boundary. The carbon grains at the outer boundary have a MRN size distribution (Mathis et al. 1977), and at the inner boundary they are completely burnt ($c_{i,j} = 0$).

The outer boundary condition of the surface density is the no-torque condition ($\Sigma = 0$), as in Paper II. However, we employ a new inner boundary condition. The physical basis and the numerical treatment of this new inner boundary condition, which we call the "quasistationary" boundary condition, is described in Appendix A. The quasistationary inner boundary condition removes the problem of an unphysical behaviour of the surface density and the temperature at the inner boundary if the no-torque condition is applied, as in the former disk model of Paper II and all other model calculations which prescribe $\Sigma = 0$ at the inner boundary. We numerically checked for the conservation of mass and angular momentum of the quasistationary boundary condition and found the mass and angular momentum of the disk to be conserved up to the numerical accuracy of the model calculations.

Table 1. Element abundances of element X relative to its solar abundance $\zeta_X = \epsilon_X/\epsilon_{X,\odot}$ (Eq. (36)) of the models with different metallicities [Fe/H] (Cols. 2–8). Column 9 shows the solar element abundances adopted in the model calculations. For details see text.

Model	S	A	B	C	D	E	F	$\epsilon_{X,\odot}$
[Fe/H]	0	0	0.2	−0.5	−1.0	−1.5	−2.0	3.24×10^{-5}
$\zeta_{\rm He}$	1.0	1.0	1.0	1.0	1.0	1.0	1.0	9.75×10^{-2}
$\zeta_{\rm O}$	1.0	1.25	1.5	0.5	0.2	0.08	0.03	4.91×10^{-4}
$\zeta_{\rm C}$	1.0	1.0	$10^{0.2}$	$10^{-0.5}$	$10^{-1.0}$	$10^{-1.5}$	$10^{-2.0}$	2.45×10^{-4}
$\zeta_{\rm Mg}$	1.0	1.25	2.0	0.5	0.2	0.07	0.025	3.85×10^{-5}
$\zeta_{\rm Si}$	1.0	1.125	1.8	0.45	0.2	0.07	0.025	3.58×10^{-5}
$\zeta_{\rm Al}$	1.0	1.25	2.0	0.5	0.2	0.03	0.003	3.04×10^{-6}

With the quasistationary inner boundary the mass transfer from the disk onto the star is determined by the mass accretion rate at the innermost point $\dot{M}_1$,

$$M_*^{t+\Delta t} = M_*^t + \dot{M}_1^t\,\Delta t \tag{40}$$

where M_*^t denotes the stellar mass at instance t, and Δt is the time step.

5.2. Numerical solution

The set of Eqs. (19)–(32) for the disk structure is solved numerically by essentially the same method as described in Paper II, but with one exception. In Paper II the calculation of the concentrations $c_{i,j}$ by means of the set of diffusion-transport-reaction Eqs. (19) was attended explicitly to the calculation of the remaining disk Eqs. (21)–(32) within a time step, i.e. the numerical method in part was explicit. As can be seen by comparison of the flow charts of the codes of Paper II and the present model (Fig. 2 in Paper II and Fig. 1 herein) the iteration of the surface density Σ now is carried out globally, i.e. including the integration of the set diffusion-transport-reaction Eqs. (19). Hence, due to this modification the numerical method now is implicit. Only the calculation of the stellar mass by Eq. (40) is done explicitly as the mass accretion onto the star occurs on the viscous timescale.

The maximum time step $\Delta t_{\rm max}$ is chosen to be 50 yr. This is somewhat smaller than $\Delta t_{\rm max}$ of the α-disk models of Paper II since we encountered some numerical instability when choosing the time step larger than ∼50 yr in the present β-disk models. However, compared to an α-disk model the CPU time for an equivalent β-disk model is reduced by a factor ∼4. This originates from the fact that in case of the β-ansatz the viscosity decouples from the thermodynamical structure of the disk (cf. Eq. (23)) causing a less problematic solution of the diffusion equation of the surface density (21). The CPU time on a P4 XEON 2.8 GHz computer for a typical 10^6 yr-disk model is about 37 min.

5.3. Models of different metallicity

The aim of the present work is to calculate models of protoplanetary disks with different metallicities. The values for the metallicities [Fe/H] and the ratios of element abundances of element X relative to solar, ζ_X (Eq. (36)), for the individual models are given in Table 1.

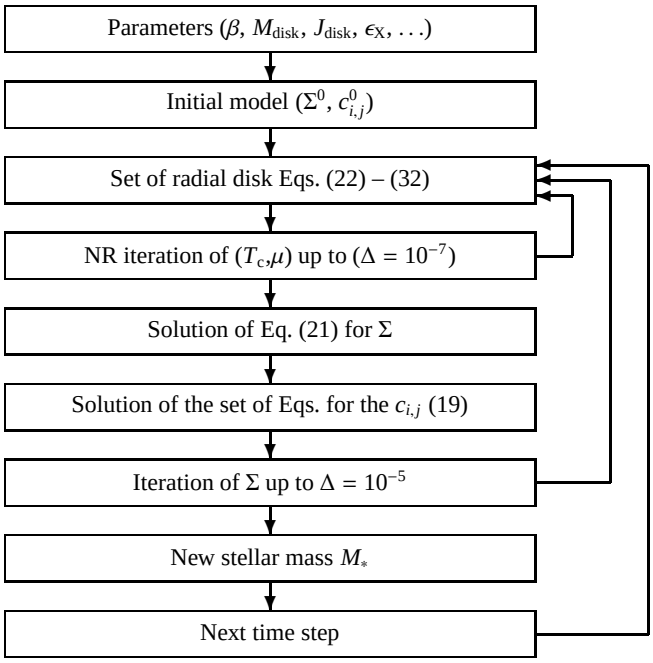

Fig. 1. Flow chart of the numerical code. The arrows to the right of the diagram denote the iteration loops and the time loop, respectively, and Δ is the accuracy of the iteration. The set of radial disk Eqs. (22)–(32) is solved by a coupled Newton-Raphson method for the midplane temperature $T_{\rm c}$ and the mean molecular weight μ.

The choice of the ζ_X is inspired by the works of Timmes et al. (1995) and Portinari et al. (1998) which compiled the element abundances of a large sample of stars in the solar neighbourhood. For a fixed metallicity their plots of element abundances versus metallicity show a large scatter of the abundances of the individual elements. This scatter is not unexpected as stars (and disks) in the galaxy form in different chemical environments with quite different evolutionary histories. To calculate models for different metallicities [Fe/H] we roughly average the individual ζ_X for given [Fe/H] from the samples of Timmes et al. (1995) and Portinari et al. (1998), respectively. In this sense the element mixtures of models A–F

(Table 1) are *typical* for stars in the solar neighbourhood for given metallicity.

In particular, model S in Table 1 corresponds to the solar element mixture. Model A corresponds to an element mixture of a typical star in the solar neighbourhood with solar metallicity. Model B is a model with a metallicity ([Fe/H] = 0.2) representing stars of present day metallicity, i.e. young stars in the solar neighbourhood. Models C – F have metallicities [Fe/H] = $-0.5 \ldots -2.0$ successively decreasing in steps of 0.5. For even lower metallicities the basic assumptions on which the model calculations are based on are no longer valid. Especially the disk then becomes vertically optically thin almost everywhere. Thus, we choose a lower limit for the metallicity of [Fe/H] = −2.0 in our model series.

It can be seen from model A in Table 1 that the sun is not a typical star within its closer environment with respect to its element mixture. The deviations of the element abundances from the mean are, however, well within the range of scattering of individual abundances. As well it follows from Table 1 that the depletion of elements with decreasing metallicity do not occur uniformly for the individual elements in typical stars close to the sun. These aspects and particularly their influence on the composition of the dust within disks will be discussed in detail in our model results (see Sect. 6). However, we already now point towards our choice of the abundances of He and C, respectively. The helium abundance is chosen to be solar in each model. The reason for this is that a variation of $\zeta_{\rm He}$ exclusively changes the mean molecular weight μ, Eq. (27), and the resulting modification of the disk models is small. The carbon abundances are chosen to decrease like the metallicities. This choice is motivated by the large scatter of the carbon abundances observed for stars in the solar neighbourhood (Timmes et al. 1995; Portinari et al. 1998), and moreover from the fact that there is no observable trend of deviations of the evolution of the carbon abundance from the evolution of the metallicity in the solar environment.

The values of the standard solar abundances of elements $\epsilon_{X,\odot}$ are taken from Anders & Grevesse (1989) (last column of Table 1), with two exceptions. Recently the abundances of carbon and oxygen of the sun are updated by more accurate model atmosphere calculations of Allende Prieto et al. (2002). The values $\epsilon_{\rm C,\odot} = 3.55 \times 10^{-4}$ and $\epsilon_{\rm O,\odot} = 7.41 \times 10^{-4}$ of Anders & Grevesse (1989) therefore are changed to the new values $\epsilon_{\rm C,\odot} = 2.45 \times 10^{-4}$ and $\epsilon_{\rm O,\odot} = 4.91 \times 10^{-4}$ of Allende Prieto et al. (2002) (Table 1). Thus the abundances of C and O both are reduced by a factor of about 1/3. This leads to a large reduction of the opacity of all species which bear C or O as the least abundant element of the compound (i.e. solid carbon, CO, OH, water vapor and ice). We found the disk structure to be significantly modified due to the updated abundances of C and O.

5.4. Model parameters

The other relevant model parameters are shown in Table 2. They are held fixed in the models of different metallicity (Table 1). The parameters of this work essentially equal the model parameters of Paper II[2].

Table 2. Parameters used for the calculation of the disk models. The stellar radius is calculated from $L_* = 4\pi R_*^2 \sigma T_*^4$.

Initial stellar mass	$M_{*,0}$	1 $M_\odot$
Stellar effective temperature	T_*	4250 K
Stellar luminosity	L_*	5 $L_\odot$
Stellar radius	R_*	4.13 $R_\odot$
Inner disk radius	$r_{\rm i}$	$5\,R_* = 0.096$ AU
Outer disk radius	$r_{\rm o}$	200 AU
Molecular cloud temperature	$T_{\rm cloud}$	20 K
Initial disk mass	$M_{\rm disk,0}$	0.2 $M_\odot$
Disk angular momentum	$J_{\rm disk}$	10^{53} g cm^2 s^{-1}
Viscosity parameter	β	10^{-5}

The viscosity parameter β is chosen to be 10^{-5} (Table 2). We did test calculations with different values for β and found the value of 10^{-5} to yield dissipation timescales for the disks in the model consistent with the evolutionary timescales of disks following from observations (e.g. Haisch et al. 2001). Interestingly, this value for β (the reciprocal critical Reynolds number of the flow) is in the range of those found by the experiments of Wendt (1933) and Taylor (1936a,b) (by a reanalysis of Richard & Zahn 1999), for turbulent flows between coaxial rotating cylinders in the limit of large gap sizes between the cylinders. In contrast, the value of β for the limit of small gap sizes, which is favoured by Duschl et al. (2000) with regard to the generation of turbulence in protoplanetary disks, β is about three orders of magnitude larger. However, we choose β such that the calculated disk lifetime is in accord with disk lifetimes deduced from observations.

6. Results

Before we discuss in detail the results of the models for different metallicities we investigate the influence of the modifications on the present model introduced in Sect. 4, as compared to Paper II.

6.1. New inner boundary condition

First we test the influence of the new inner boundary condition. To do this we compare two models: (1) a model with the no-torque inner boundary condition ($\Sigma_1 = 0$) as it has been applied in Paper II, and (2) a model including the new quasistationary inner boundary condition (see Appendix A). Both models are calculated with the α-viscosity description, without including

[2] Note that an error occured in Paper II regarding the estimation of the disk angular momentum by means of the relation of Stepinski (1998), $J_{\rm disk,ste} = 6.7\alpha^{0.34}$ (see Eq. (39) of Paper II). This relation refers to the lower branch of solutions for $J_{\rm disk}$ in the work of Stepinski (1998), and the values given in Table 2 of Paper II actually are in units of 10^{52} g cm^2 s^{-1}, hence one order of magnitude smaller. For the upper branch of solutions for $J_{\rm disk}$ in Stepinski (1998) there holds $J_{\rm disk,ste} = 46\alpha^{0.28}$ which, however, leads to a value of $J_{\rm disk,ste}$ of the same order of the values given in Table 2 of Paper II.

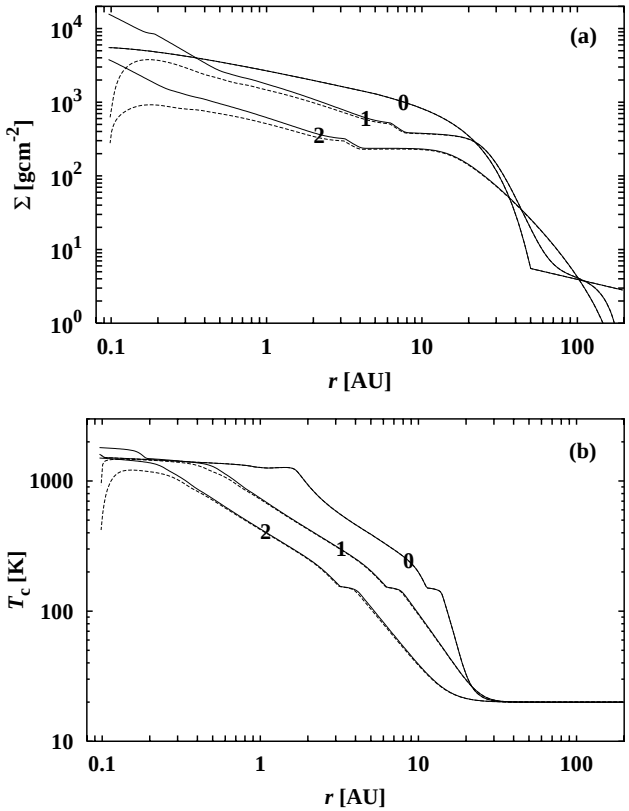

Fig. 2. Radial structure of an α-disk model with the quasistationary inner boundary condition (solid lines) compared with an α-disk model with the no-torque inner boundary condition (dashed lines) at $t = 0$ (0), 10^5 (1) and 10^6 yr (2). **a)** Surface density Σ. **b)** Midplane temperature T_c.

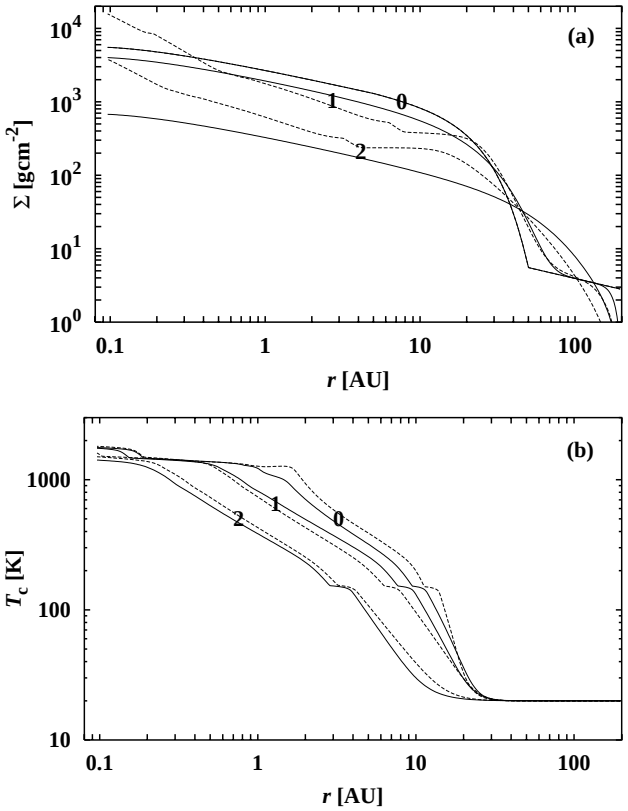

Fig. 3. Radial structure of a β-disk model (solid lines) compared with an α-disk model (dashed lines) at $t = 0$ (0), 10^5 (1) and 10^6 yr (2). **a)** Surface density Σ. **b)** Midplane temperature T_c. Note that the initial temperature structure of both models is different due to the different viscosity prescriptions.

selfgravitation of the disk and with a solar element mixture. In either case the initial model is that of model S, and $\alpha = 3{\times}10^{-3}$.

The results are shown in the plots of the surface density Σ and the midplane temperature T_c versus the radial distance r to the star in Fig. 2. It is obvious that the more realistic quasistationary inner boundary condition strikingly modifies the disk structure compared to the no-torque inner boundary condition, in spite of previous assertions that the no-torque inner boundary condition has only small influence on the disk structure. The surface density Σ (Fig. 2a) at 0.2 AU after 10^6 yr in the no-torque model is unphysically reduced by a factor of ∼2, and at 1 AU still by a factor of ∼1.2. As well, the modification of the thermal structure is significant. The midplane temperature T_c (Fig. 2b) of the "quasistationary" model compared with the no-torque model at 10^6 yr is reduced from 1380 K to 1180 K at 0.2 AU, but only from 428 K to 423 K at 1 AU, respectively. Differences of T_c of the order of 100 K in the inner portions of the disk are quite important, since chemical processes react quite sensitive even on small temperature variations. The artificial reduction of T_c due to the $\Sigma = 0$ inner boundary condition extending outwards up to ∼1 AU is not acceptable, if chemical processes and dust processing in the disk are to be modeled.

Owing to these findings we strongly recommend the application of the quasistationary inner boundary condition to each time dependent disk model in the one-zone approximation. The extra computational expense we found to be only small since the calculation of the new quasistationary boundary condition has to be done at only one radial point, at the inner boundary, as described in Appendix A. Moreover, large gradients close to the inner edge as they occur in case of the no-torque condition are avoided. Note also the smooth inward "lapse" of Σ and T_c at the inner edge in the model with the quasistationary inner boundary condition in Fig. 2.

6.2. α versus β

Next we investigate the effect of the β-viscosity. For this purpose we compare (i) a model with α-viscosity with (ii) a model with β-viscosity. Both models are computed with the quasistationary inner boundary condition, without including selfgravity of the disk and with solar element mixture. In both cases the initial model is that of model S. The viscosity parameters are $\alpha = 3 \times 10^{-3}$ and $\beta = 10^{-5}$.

The results are shown in Fig. 3. As previously noted, in β-disk models the evolution of the surface density Σ decouples from the thermal structure of the disk. Hence, the radial distribution of Σ in the β-disk model is "smooth" (Fig. 3a) whereas the surface density in the α-disk model reflects the kinks of the thermal structure (Fig. 3b). The thermal structure does not change much if turning from the α- to the β-prescription of the viscosity (Fig. 3b). The most distinct influence on the disk structure has the choice of the value of β (or α) as this

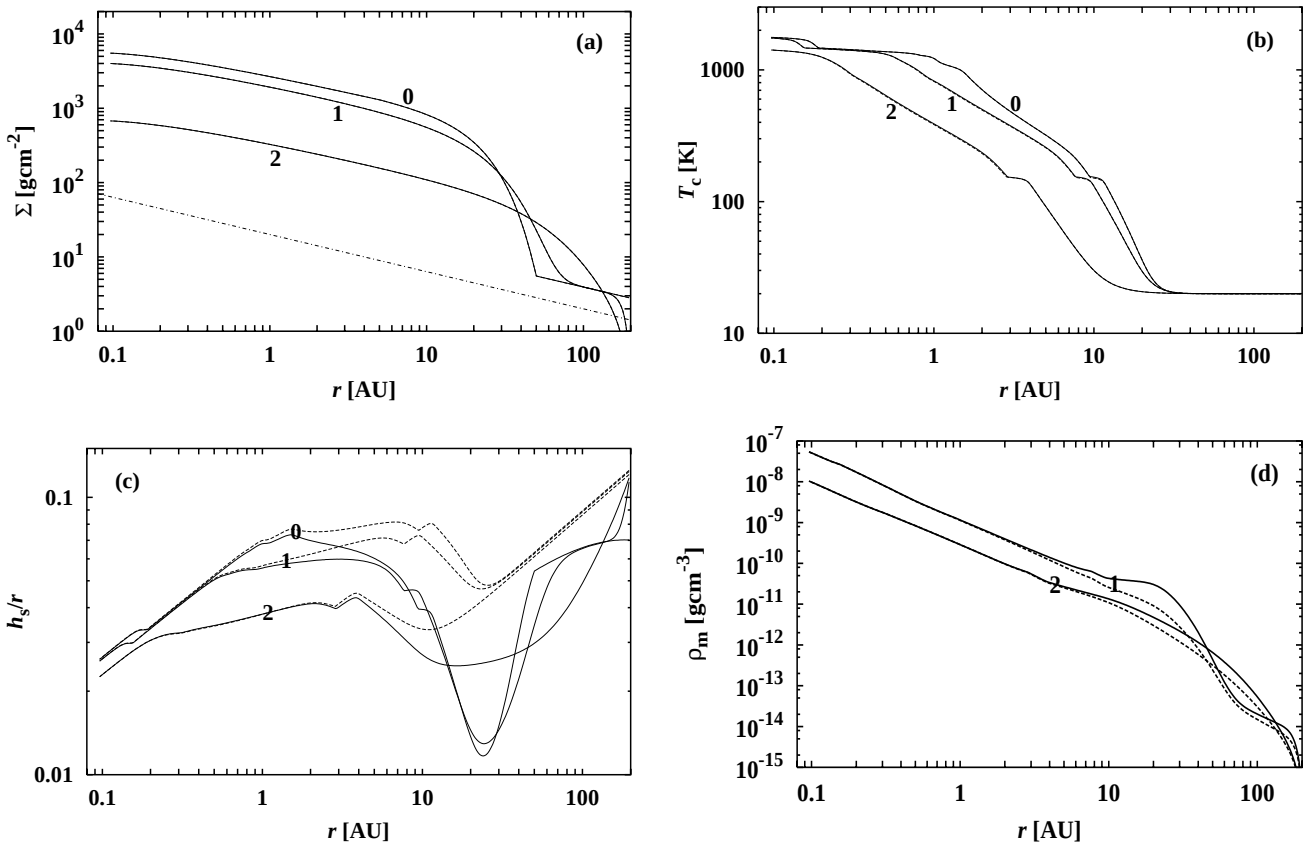

Fig. 4. Radial structure of a β-disk model including (solid lines) and excluding (dashed lines) vertical selfgravitation of the disk at $t = 0$ (0), 10^5 (1) and 10^6 yr (2). **a)** Surface density Σ. The dot-dashed line is a curve with $\Sigma \propto r^{-0.5}$ which represents the run of the surface density for a stationary β-disk model. **b)** Midplane temperature T_c. **c)** Aspect ratio h_s/r. **d)** Vertical averaged density ρ_m. The initial density profile is not shown in this case for clarity. Note that the initial radial profiles of T_c, h_s/r and ρ_m of models including selfgravity differ from the corresponding radial profiles of models neglecting selfgravity. The radial profile of the surface density Σ, in contrast, is the same in either cases since it is fixed by the initial disk mass and initial angular momentum.

determines the evolutionary timescale of the disk. In our case of $\beta = 10^{-5}$ the mass accreted onto the star in this model amounts to $7.1\times10^{-2}\,\dot{M}_\odot$ after 10^6 yr whereas it is $6.0\times10^{-2}\,\dot{M}_\odot$ for the $\alpha = 3\times10^{-3}$ model. Note that the initial temperature structures of the models with α- and β-viscosity are different due to the different viscosity prescriptions.

6.3. Selfgravity of the disk

Finally, we turn to the vertical selfgravitation of the disk (see Sect. 4.1) by comparing (i) a model excluding the vertical selfgravitation of the disk with (ii) a model including the disk's vertical selfgravity. Both models are computed with the quasistationary inner boundary condition and with solar element mixture. Hence case (ii) equals model S (Table 1).

The results are shown in Fig. 4. As can be seen the inclusion of vertical selfgravity of the disk has no influence on the radial distribution of the surface density Σ (Fig. 4a). This once again reflects the decoupling of the evolution of Σ from that of the temperature T_c in models of β-disks, and hence the decoupling of Σ from h_s which is the quantity in which the present description of the vertical selfgravity enters in the model calculations (Eq. (25)). For comparison in Fig. 4a also the profile of the surface density following from the solution of the stationary problem ($\partial\Sigma/\partial t = 0$; $\Sigma \propto r^{-0.5}$) is shown (dot-dashed line). In the inner parts of the disk the surface density distribution becomes flatter as compared to the stationary case due to the influence of the time dependent accretion process.

The midplane temperature T_c (Fig. 4b) is only slightly modified if turning on selfgravity. The reason for this is the slight dependence of T_c (Eq. (32)) on the pressure scale height h_s, i.e. on the the disk's selfgravity, since the viscous dissipation rate $\dot{E}_\nu$ (Eq. (30)), which mainly determines T_c, only contains quantities which are independent of the temperature structure of the disk (Ω, ν, Σ). The small discrepancy of the midplane temperature between the models including and neglecting selfgravitation of the disk are due to the optical depth $\tau_{R/P}$ (Eq. (29)), i.e. the opacity of the disk matter $\kappa_{R/P}$ (Eq. (28)).

The aspect ratio h_s/r is strongly modified if vertical selfgravitation of the disk is included in the model calculations (Fig. 4c). The reason for this is that in the outer parts of the disk the disk's vertical selfgravity becomes dominant over the vertical component of the star's gravity, as clearly can be seen by the downwards bump of the aspect ratio in Fig. 4c. This "dip" of the aspect ratio extends from ∼1 to ∼80 AU at 10^5 yr, changes its location with time, and extends from ∼4 AU to the outer edge (200 AU) at 10^6 yr as a consequence of the viscous

spreading of the disk matter with time. At the location of the gap the disk surface should be strongly shadowed from the irradiation of the central star, and thus the disk may cool down in this region. However, we have not included the effect of disk heating by irradiation from the central star up to now since this requires 2D radiative transfer calculations which are out of the scope of the present work. Note that the pressure scale height provides no information about the height where the radiation of the star actually penetrates the disk surface and how the scattered stellar radiation diffuses into the disk interior.

In contrast to the surface density (Fig. 4a), the *density* (Fig. 4d) is strongly affected by the disk's selfgravitation since $\rho_{\rm m}$, the vertical averaged density in our model, is determined by the pressure scale height $h_{\rm s}$ (Eq. (26)). $\rho_{\rm m}$ increases by a factor of ~3.6 at 25 AU after 10^5 yr if selfgravitation of the disk is considered. The modification of the density structure by selfgravity is most pronounced in the cool outer parts of the disk outwards of the condensation front of water ice where chemical reactions are slow. Hence selfgravity mainly should influence the chemistry in the cool outer disk regions, e.g. the freezeout of molecules onto grains. Such calculations are out the scope of this work.

Note that the impact of the vertical selfgravitation on the disk structure, i.e. the dip of the scale height and the increase of the midplane density, was already observed by Hure (2000).

With regard to radial mixing the outward transport of matter in the model including vertical selfgravity is slightly impeded compared to the model neglecting vertical selfgravity because the density gradient becomes flatter in the zone of vertical selfgravitation (Fig. 4d).

We note that the effect of selfgravity on the disk structure varies with the disk mass $M_{\rm disk}$. In the present models we assume rather massive disks with initially $M_{\rm disk} = 0.2\,M_\odot$ which represent the upper tail of the distribution of disk masses of *evolved* disks (e.g. Natta 1999). Such a large value for the disk mass is probably not unusual immediately after the formation of the disk (Nakamoto & Nakagawa 1994, 1995). To evaluate the effect of selfgravity we perform some test calculations with different initial disk masses and angular momenta (not shown). The initial angular momentum of the disk scales linear with the initial disk mass in these test calculations. We observe a significant modification of the disk structure by selfgravity down to a disk mass of $M_{\rm disk} = 0.02\,M_\odot$. Thus a large fraction of the observed protoplanetary disks should be affected by the selfgravitation of the disk. Hence, if one wants to omit the numerical effort of solving the Poisson equation to take into account the full selfgravitation of the disk, at least the disk's *vertical* selfgravity ought to be considered within models of protoplanetary disks.

In the following we present the results of calculations of models with different element mixtures and discuss them.

6.4. Model A

First we look at the results of model A, the model of a protoplanetary system with a typical element mixture as encountered in the solar neighbourhood (Table 1). We compare this model to model S with solar composition.

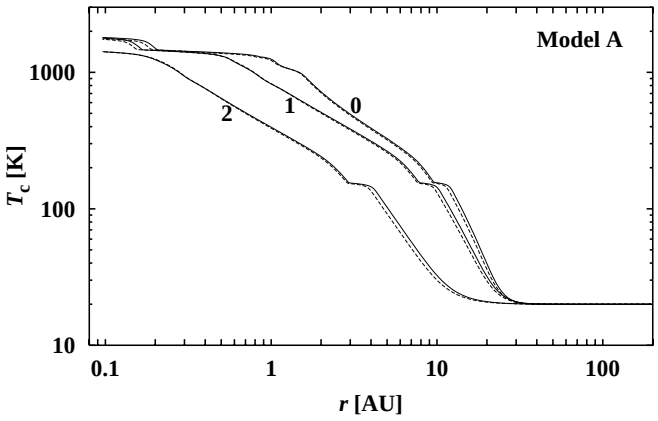

Fig. 5. Evolution of the midplane temperature $T_{\rm c}$ in model A (solid lines) compared with the "solar" model S (dashed lines) at $t = 0$ (0), 10^5 (1) and 10^6 yr (2). The initial models are already different due to the different element compositions.

Figure 5 shows the result for the temperature profile of the disk in both models. The midplane temperature $T_{\rm c}$ of model A does not show strong modifications as compared to the solar abundance model S. This can be explained by the fact that due to equal metallicities in both models the chemical composition is similar *on average*.

The radial profile and evolution of the surface density of model A equals that in Fig. 4a because, as we already noted, the evolution of Σ is not affected by the thermal evolution of the disk. For given disk mass $M_{\rm disk}$ and disk angular momentum $J_{\rm disk}$, 0.2 $M_\odot$ and 10^{53} g cm^2 s^{-1} in each of the models A–F, respectively, the evolution of the surface density Σ is determined exclusively by Eqs. (21)–(23) and the inner boundary condition (Appendix A).

A good way to compare the models of different element mixture is to plot the opacity profile of the individual absorbers of the disk. The Rosseland mean of the opacity versus the radial axis of models A (solid lines) and S (dashed lines) at 10^5 yr are shown in Fig. 6[3].

First of all in Fig. 6 one can observe what is common to all the models presented here (see also the other Papers of this series): different species represent the main absorbers within different temperature ranges in the disk, that are

- ice mantled grains up to $T_{\rm c} \sim 155$ K,
- amorphous silicate grains in the range $155\,{\rm K} \lesssim T_{\rm c} \lesssim 500\,{\rm K}$,
- carbon grains at $500\,{\rm K} \lesssim T_{\rm c} \lesssim 1100\,{\rm K}$,
- iron grains at $1100\,{\rm K} \lesssim T_{\rm c} \lesssim 1450\,{\rm K}$,
- corundum grains at $1450\,{\rm K} \lesssim T_{\rm c} \lesssim 1800\,{\rm K}$ and
- molecules (mainly H_2O) above $T_{\rm c} \sim 1800$ K,

respectively. At higher temperatures also ions and electrons contribute to the opacity, but the present disk models do not reach such large temperatures at the inner edge.

[3] We use the Rosseland mean of the opacity $\kappa_{\rm R}$ instead of the Planck mean $\kappa_{\rm P}$ for the presentation of the results, as in Paper II, since the disks are optically thick in the regions of interest, i.e. in the chemical active zones.

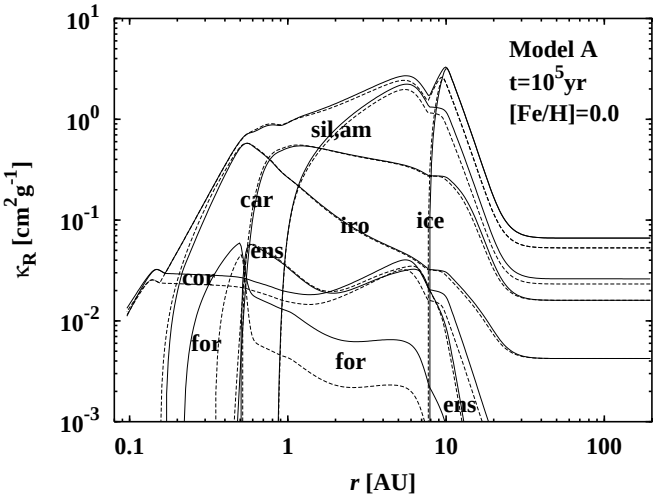

Fig. 6. Radial dependence of the Rosseland mean of the opacity κ_R in model A (solid lines) and model S (dashed lines) at 10^5 yr. The thick lines represent the total opacities of the models whereas the thin lines show the opacity of the individual absorbers as labeled by abbreviations.

The most important modifications between models A and S results from the different oxygen abundances. Model A for a typical star (and disk) in the solar vicinity has 1.25 times the solar abundance of oxygen (Table 1). This results in two major modifications of model A as compared to the solar abundance model S (Fig. 6): first, the ice abundance is enhanced since there simply is more oxygen to form H_2O. Therefore, in model A the opacity in the region of ice stability increases as compared to model S. Second, the abundance of OH molecules is enhanced. Hence, the combustion of carbon grains, which mainly depends on the particle density of OH (see Papers I and II), becomes more efficient, and the carbon combustion front is shifted outwards to lower temperatures in model A as compared to model S.

A further important feature when comparing models A and S is the dependence of the composition of the silicate component on the ratio of magnesium-to-silicon abundance $\epsilon_{\rm Mg}/\epsilon_{\rm Si}$. In the solar case this ratio is close to unity, $\epsilon_{\rm Mg}/\epsilon_{\rm Si} = 3.85 \times 10^{-5}/\, 3.58 \times 10^{-5} = 1.075$. As a consequence silicate occurs mainly in the form of enstatite rather than forsterite in the solar nebula model S in the region where both dust species are stable under equilibrium conditions, i.e. for temperatures lower than about ∼1310 K (Figs. 5 and 6). The reason for this is the competition between the higher stability of forsterite than of enstatite and the requirement to condense Mg and Si as complete as possible into solids. Since forsterite binds two Mg atoms but enstatite only one, for low Mg/Si abundance ratios enstatite formation is favoured, while for high Mg/Si abundance ratios forsterite formation is favoured. This can be seen in model S (Fig. 6, dashed lines) where the abundance of enstatite is ∼12 times the forsterite abundance below ∼1310 K (for $r \gtrsim 0.5$ AU at 10^5 yr). If the ratio of magnesium to silicon abundance is increased, as is the case in model A (Fig. 6, solid lines) with $\epsilon_{\rm Mg}/\epsilon_{\rm Si} = 1.195$, more Mg is available to be bound in forsterite, and the ratio of enstatite to forsterite grains in model A decreases to about 4. Nevertheless, our model calculations predict enstatite to be significantly more abundant than forsterite in typical disks in the solar neighbourhood with the same metallicity as the solar system.

Above ∼1310 K under the conditions of protoplanetary disks enstatite becomes unstable and transforms into forsterite. In model A forsterite is more refractory against vaporization as compared to model S. In model A the last forsterite grains disappear at ∼1440 K whereas in model S they do already at ∼1390 K (Figs. 5 and 6). The reason for this is, again, the enhanced abundances of O, Mg, and Si in model A as compared to model S.

The opacity of the crystalline silicate (forsterite and enstatite) does only little contribute to the total opacity. As already discussed in Paper II the opacity of crystalline silicates is by an order of magnitude lower as compared to amorphous silicates which determine the thermal structure of the outer parts of the disk, where they represent the dominant absorber inside of the ice condensation front. However, the opacity decreases in the outer parts of the disk with time as crystalline silicates, which originate from annealing of amorphous silicates in the inner parts of the disk, are mixed radially outwards. Figure 6 shows that after 10^5 yr silicate grains are mixed outward up to $r > 10$ AU. Enstatite grains are more numerous than forsterite grains since the former are formed in higher quantities. With regard to the formation of solar system bodies this means that the crystalline silicates observed in comets should be present mainly as enstatite rather than forsterite. For a discussion of this aspect we refer to our conclusions (see Sect. 8).

The process of radial mixing in the present model is independent of the element mixture. This is explained by the fact that radial mixing occurs on the viscous timescale, and the β-viscosity applied in our model calculations is independent of the thermal (and therefore opacity) structure of the disk. The slightly larger opacity of enstatite in the region outwards of the ice front in model A as compared to model S is due to the dependence of the enstatite opacity on the temperature, but not a consequence of a different efficiency of radial mixing due to the different element mixtures between both models.

Finally, the enhanced aluminum abundance in model A as compared to model S (Table 1) leads to a larger abundance of corundum in model A. This modifies the structure of the innermost parts of the disk since corundum is the most refractory dust species considered in our model calculations.

6.5. Model B

The metallicity in this model is chosen to represent an extreme case of high metallicity in a star-disk system in the solar neighbourhood, [Fe/H] = 0.2. The abundances of elements other than Fe are typical for a star with this metallicity close to the sun (Timmes et al. 1995; Portinari et al. 1998), as described above and shown in Table 1. The opacity structure of the disk model B at 10^5 yr is shown in Fig. 7.

As can be seen in Fig. 7 the total opacity of the disk matter in model B (thick solid line) compared to the solar abundance model S (thick dashed line) roughly increases by the same factor as the metallicity increase, i.e. by a factor ∼1.6. This is

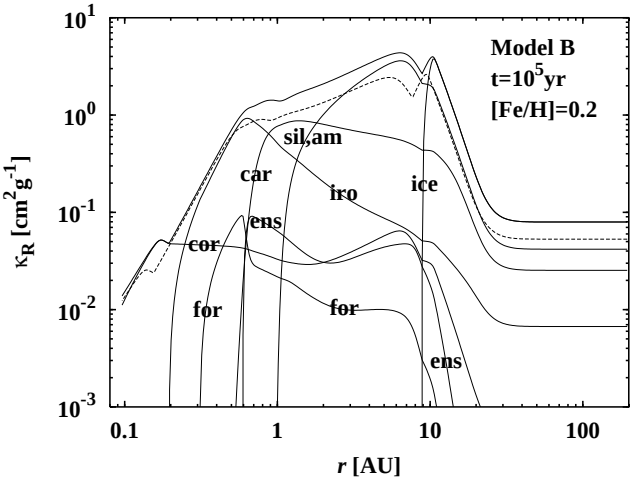

Fig. 7. Radial dependence of the Rosseland mean of the opacity κ_R in model B (solid lines) and model S (dashed line) after 10^5 yr. The thick lines represent the total opacities of either models whereas the thin solid lines show the opacity of the individual absorbers in model B as labeled by abbreviations.

because the abundance of carbon varies as the metallicity in our models, and since extinction by soot dominates the opacity in the region around 1 AU after 10^5 yr in model B. Similarly, in the outer parts of the disk, where ice coated grains dominate the opacity, the opacity increases. This is a consequence of the oxygen abundance in model B as compared to model S which increases only slightly less than the carbon abundance with increasing metallicity, i.e. by a factor 1.5. Hence, the abundance of ice in model B is only about 1.5 times the ice abundance of model S.

In contrast to the oxygen abundance, the abundances of the silicate forming elements Mg and Si increase stronger with increasing metallicity. This leads to a larger opacity of amorphous as well as crystalline silicates in model B compared to model S. The maximum value of the opacity of amorphous silicate becomes as large as the maximum value of the ice opacity. As well, in model B the abundance of annealed silicates increases compared to model S, and more crystalline forsterite and enstatite is mixed outwards. The ratio of abundances of Mg to Si do not change compared to model A, so the ratio of forsterite to enstatite grains remains at the level of model A.

The higher metallicity of model B compared to model S of course also enlarges the abundance of iron grains, and therefore the contribution of solid iron to the total opacity is increased. As well aluminum has a higher abundance (cf. Table 1) which clearly can be seen at the offset of the corundum opacity in model B.

6.6. Models C–F

The models C, D, E and F, respectively, are cases of typical protoplanetary star-disk systems in the solar vicinity with successively lower metallicities ([Fe/H] = −0.5, −1.0, −1.5 and −2.0, respectively) and accordingly lower abundances of element other than Fe (Table 1). The total opacities and the opacity profiles of the individual absorbers of models C – F at 10^5 yr are shown in Fig. 8.

The most striking feature of models C – F is the drop of the total opacity with decreasing metallicity, as can be seen in Fig. 8, where each plot also shows the total opacity of the solar abundance model S (dashed lines) for comparison. The total opacity decreases roughly to the same extent as the metallicity decreases, e.g. in model F with [Fe/H] = −2.0 the total opacity is about two orders of magnitude lower as compared to model S.

Superimposed to the overall decrease of κ_R with decreasing [Fe/H] are the intrinsic changes of the ratios of the abundances of the dust forming elements in models C – F which result in modifications of the opacity and abundance of the individual dust species. For example, in model C the ratio of abundances of Mg to Si is enlarged as compared to solar abundance (same value as in models A and B) whereas it is solar in models D, E and F, respectively. This leads to the same conclusion as found for models A and B (Sects. 6.4 and 6.5): with increasing $\epsilon_{Mg}/\epsilon_{Si}$ forsterite becomes more abundant at the expense of enstatite.

We remark that the scatter of the Mg-to-Si ratio around the mean of stars in the solar vicinity yields unusual enstatite-to-forsterite ratios in some disks. For example, a Mg-to-Si ratio of 1.5 leads to equal abundances of enstatite and forsterite, whereas for $\epsilon_{Mg}/\epsilon_{Si} \leq 1$ forsterite is not stable under equilibrium conditions and silicon is bound in enstatite and quartz.

With decreasing metallicity iron is more depleted than other important dust forming elements such as O, Mg and Si, with exception of C which, as already noted, changes like the metallicity in the present model. This has the consequence that the abundance of iron grains decreases super-proportionally compared to other condensates when going from model C to model F. Hence the solid iron opacity contributes less to the total opacity in model F, particularly in the inner zones of the disk, since solid iron is the last but one dust species which disappears.

Somewhat surprising is that carbon grains survive up to higher temperatures in models with lower as compared to higher metallicity. In the present models the abundance of carbon changes in accord with the iron abundance, and the carbon abundance relative to the abundances of O, Mg and Si decreases the more the metallicity decreases. Therefore one would expect a deficit of carbon grains in the low as compared to the high metallicity models. However, at 10^5 yr a degree of condensation of carbon into carbon grains of $f_{car} = 0.1$ in model C is attained at a midplane temperature of ∼1065 K ($r = 0.52$ AU) whereas in model F $f_{car} = 0.1$ is reached at $T_c \sim 1255$ K ($r = 0.14$ AU). This can be explained as follows: the particle density of OH molecules decreases with decreasing O abundance, i.e with decreasing metallicity. As a consequence carbon grains can penetrate to regions of higher temperature in low compared to the high metallicity models before they are destroyed by OH. Therefore the carbon combustion front in low metallicity models is shifted to higher temperature as compared to high metallicity models.

The change of the aluminum abundance with metallicity resembles that of O, Mg and Si, except for models E and F with lowest metallicities. For [Fe/H] $\lesssim$ −1.5 the Al abundance

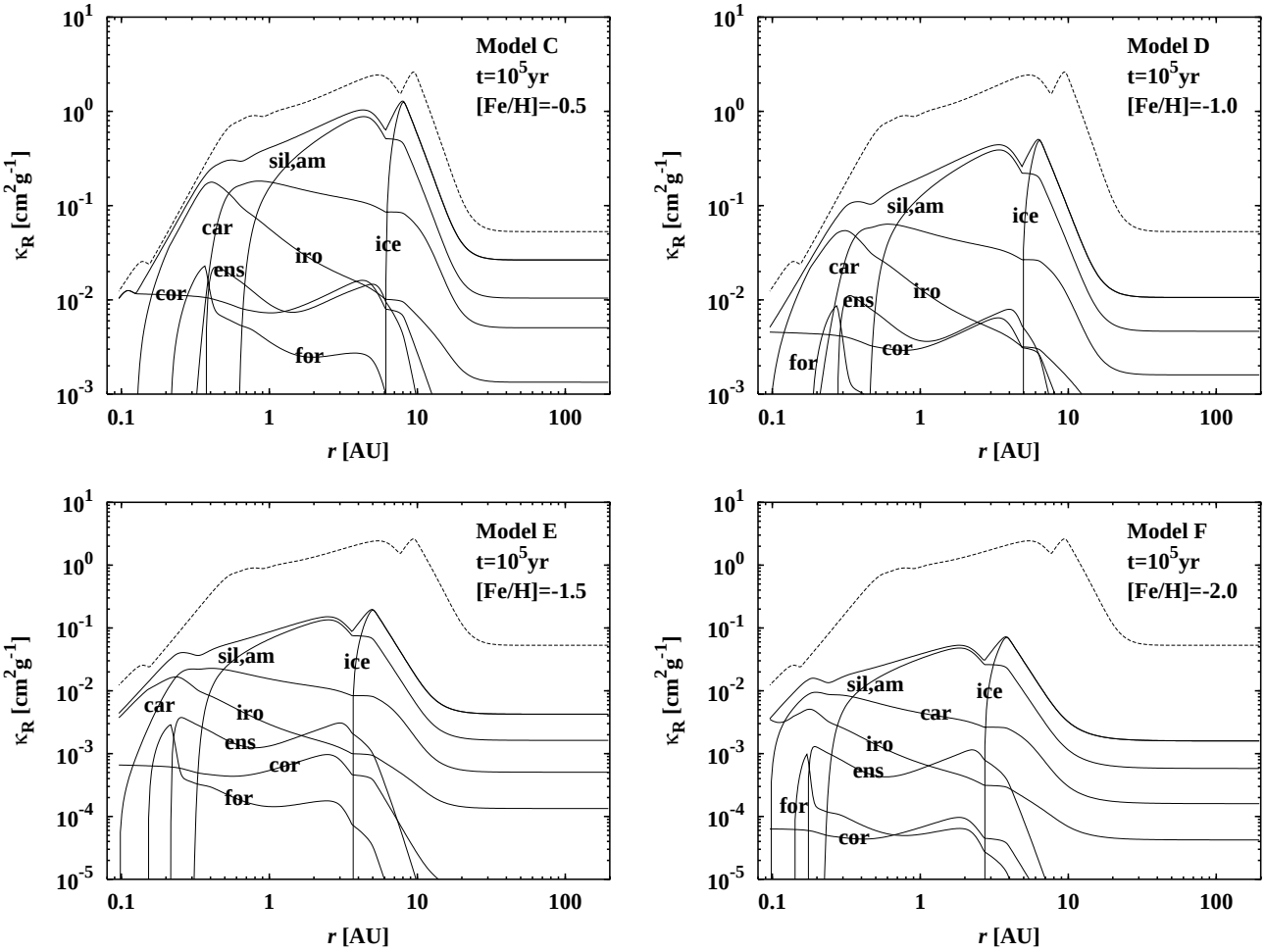

Fig. 8. Same as Fig. 7, but **a)** for model C, **b)** for model D, **c)** for model E and **d)** for model F, respectively. Note the enlargered range of the vertical axis in the plots of models E and F compared to models C and D.

decreases super-proportional with decreasing metallicity in typical stars of the solar neighbourhood (Timmes et al. 1995), pointing to a so far unknown source of Al in the chemical evolution of the galaxy. In models E and F corundum therefore becomes less important for the total opacity balance. This is also due to the fact that the low as compared to the high metallicity models are generally cooler as a consequence of the reduced opacity although the initial mass and angular momentum for all models is the same. Hence, the lowest metallicity models E and F never reach temperatures of ∼1450 K in their evolution at the inner edge above which corundum grains become the dominant absorbers.

As the temperature in the disk decreases with decreasing metallicity outward radial mixing of matter is curtailed. E.g., at 10 AU after 10^6 yr in model C the fraction of crystalline enstatite $f_{\rm cry,ens}$ reaches 7.3% while in model F at the same location and time $f_{\rm cry,ens}$ = 3.3%. Superposed to the diffusive spread of the disk is the advection of matter towards the star in the inner and intermediate parts of the disk. In late phases of disk evolution this inward drift overcomes the outward diffusive mixing, and therefore the crystalline silicates experience a net inward drift at this time. As a consequence the fraction of crystalline silicate at a fixed radius outwards of ∼10 AU first increases in the early phase of disk evolution due to radial mixing, then takes its maximum value, and finally decreases by the inward drift of the disk matter.

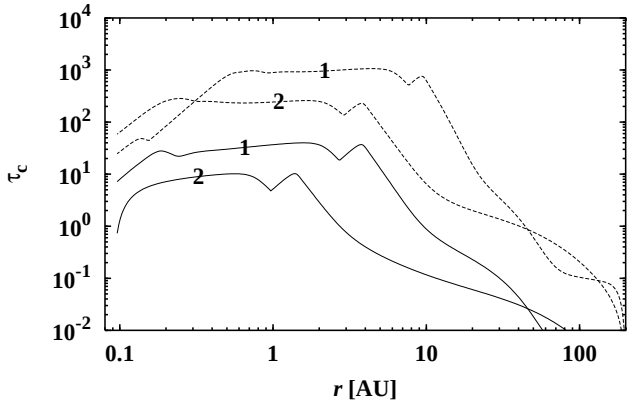

Fig. 9. Rosseland vertical optical depth $\tau_{\rm R}$ of model F (solid lines) and model S (dashed line) at 10^5 (1) and 10^6 yr (2).

Finally, Fig. 9 shows the radial dependence of the Rosseland mean vertical optical depth $\tau_{\rm R}$ of model F (solid lines) compared to the solar model S (dashed lines) after 10^5

and 10^6 yr, respectively. One can see that the lowest metallicity model F exhibits optical depths larger than unity until 10^6 yr at least within the inner 3 AU of the disk where the most important chemical processes occur. Protoplanetary disks with zero metallicity below ∼3000 K are vertically optically thin (Duschl & Mayer 2003, in preparation) since dust in these disks is absent and the sole absorbers are H and He. We conclude that protoplanetary disks of masses of about a tenth of the sun become optically thin for all times roughly below [Fe/H] = −4.0. For lower disk masses, however, this limit for the metallicity shifts to larger values.

6.7. Distribution of solid matter in the disk models of different metallicity

Figure 10 shows the radial dependence of the dust-to-gas mass ratio $f_{\rm dust:gas}$ of the solar abundance model S (top) and the model with lowest metallicity, [Fe/H] = −2.0, model F (bottom), after 10^5 yr of disk evolution. Also shown are the cumulative contributions of the individual dust species to $f_{\rm dust:gas}$. As can be seen, the gas-to-dust ratio in the zone of terrestrial planets in the solar model S after 10^5 yrs is ∼200, and significantly decreases below 100 as soon as the conditions allow ice condensation ($f_{\rm dust:gas} \approx 0.0117$), i.e. more than one half of the mass of the condensates is in form of ice within the "icy" region of the disk. The other half of the mass of the condensates is distributed among carbon, silicate and iron grains roughly in the ratio 1:2:1. Corundum has only a minor contribution to the total condensed mass but, as already mentioned, is important for the structure of the innermost parts of the disk since it is the last condensate that disappears.

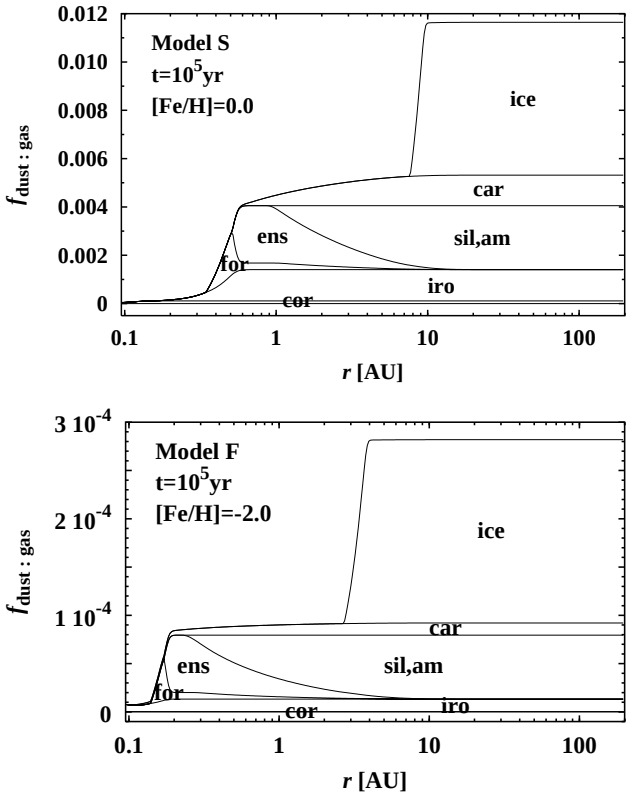

Fig. 10. Cumulative plot of the dust-to-gas mass ratios $f_{\rm dust:gas}$ of the individual dust species versus radial distance r of the solar abundance model S (top) and the model F with lowest metallicity, [Fe/H] = −2.0, (bottom) after 10^5 yr of disk evolution. The individual dust species are labeled by obvious abbreviations.

As compared to the solar abundance model S (Fig. 10, top) the lowest metallicity model F (Fig. 10, bottom) exhibits a by a factor of ∼50 smaller abundance of condensed matter. This factor is smaller than 100, i.e. smaller than the value one would expect from the value of metallicity of −2.0 in model F, since Fe and C are less abundant relative to O and Si in this model as compared to the solar reference model S. This is attributed to supernovae of type Ia and AGB-stars that produce much Fe and C, respectively, only in the late stages of the galactic chemical evolution, and furthermore attributed to the evolution of the abundance of C that does not deviate much from the evolution of the Fe abundance in the galactic neighbourhood of the sun (e.g. Portinari et al. 1998; cf. Table 1). As a consequence in model F ice contributes about 2/3 to the mass balance of the condensates outwards the snow line, and the mass ratio of carbon to silicate to iron grains is roughly 1:6:1. As well as Fe also Al achieves its present-day abundance not until late times of the chemical evolution of the galaxy, hence the mass fraction of corundum relative to the other condensates in model F is clearly lowered compared to model S.

Figure 10 shows, again, the remarkable extent of outward radial mixing of the crystalline silicates which have been annealed in the inner parts of the disk. At the same time amorphous silicates are depleted in the inner region of the disk. In the present work the silicates are divided into crystalline forsterite, crystalline enstatite and amorphous silicates originating from the ISM, respectively. A more detailed discussion of the silicate chemistry, including iron bearing silicates and quartz, is given in Paper IV.

Figure 10 shows, again, the radial inward shift of the condensations fronts of the individual dust species in the low metallicity model F (bottom) as compared to solar metallicity (model S, top) that results from the fact that low metallicity disks are cooler than their high metallicity counterparts.

Figure 11 shows a plot of the surface density $\Sigma_{\rm d}$ of the condensed matter at the location of ice condensation (90% of the available oxygen locked up in ice) versus the metallicity [Fe/H] at 10^5 (boxes) and 10^6 yr (crosses) for the models of different metallicity. Also plotted in Fig. 11 with a dashed line is the value $\Sigma_{\rm d} = 20\,{\rm g\,cm^{-2}}$ at the location of the snow line which is found to be required for the formation of Jupiter within 10^6 yr (Lissauer 1987; Wetherill 1989). These authors assumed the nucleated instability as the process of formation of giant gaseous planets. The main argument for this estimate is that Jupiter must have formed fast enough to stir up the orbits of the planetesimal at the present location of the asteroid belt and inhibit the formation of a planet there. It can clearly be seen that none of the present models reaches the critical surface density of dust and ice found by Lissauer (1987) and Wetherill (1989), respectively, for the formation of Jupiter.

This is in part a consequence of the depletion of the disk matter with time by accretion which, to our knowledge, is

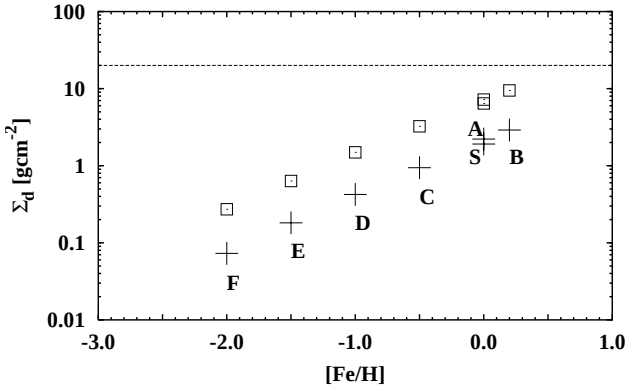

Fig. 11. Surface density Σ_d of the condensed matter (dust and ice) at the location in the disk where the degree of condensation of ice f_{ice} has the value 0.9 versus the metallicity [Fe/H] at 10^5 (boxes) and 10^6 yr (crosses) for the models of different metallicity (denoted by capitals). The dashed line represents the critical value for Σ_d of $20\,\mathrm{g\,cm^{-2}}$ of the minimum surface density of condensed material at the snow line which found to be required for the formation of Jupiter within 10^6 yr (Lissauer 1987; Wetherill 1989).

not taken into account in models of giant planet formation by the nucleated instability so far (for a recent model see, e.g., Thommes et al. 2003). The disks in the present model initially are rather massive in fact, $M_{\rm disk} = 0.2\,M_*$, which corresponds to ten times the minimum-mass model of the solar nebula (Hayashi 1981), but have lost almost one half of their mass after 10^6 yr. The extent of the depletion of disk matter in turn depends on the viscosity, i.e. the value of β which is 10^{-5} in all simulations. To realize a disk that exceeds the critical $\Sigma_d = 20\,\mathrm{g\,cm^{-2}}$ at the snow line at least until 10^5 yr of disk evolution the disk mass has to be of the order of the stellar mass. Such a disk should likely to be gravitationally unstable in its outer parts since the Toomre parameter (Toomre 1964) becomes less than unity there.

On the other hand the distribution of mass within the disk depends on the disk angular momentum. Choosing a lower initial disk angular momentum results in the deposition of more mass in the inner and intermediate disk parts, and more condensed material at the location of the snow line will be available then. However, we found in test simulations the effect on the surface density of condensed matter at the ice front to be small when varying the initial angular momentum. To obtain $\Sigma_d = 20\,\mathrm{g\,cm^{-2}}$ the disk angular momentum has to be about ten times smaller than $J_{\rm disk} = 10^{53}\,\mathrm{g\,cm^2\,s^{-1}}$, the value chosen for the present model calculations. The disk angular momentum then is similar to that of the Hayashi (1981) minimum-mass model of the solar nebula, but for a disk with a mass of ten times the Hayashi (1981) minimum-mass model, i.e. $M_{\rm disk} = 0.2\,M_*$. This seems to be unrealistic for such a massive disk.

The above results possibly impose strong constraints on the formation process of the gaseous planets in our and other planetary systems. We will discuss this issue in the conclusions (Sect. 8).

7. Summary

In the present paper we performed time dependent model calculations of protoplanetary accretion disks in the one zone approximation with different element mixtures. The metallicities of the models range from super-solar, [Fe/H] = 0.2, down to 1% of solar metallicity, [Fe/H] = −2.0. Particular attention has been given to a realistic modeling of the dust metamorphosis within the model. For this reason the model includes the condensation of the most abundant dust species in chemical equilibrium in the inner part of the disk, a realistic opacity description of the disk matter, and radial mixing processes of dust species. The results can be summarized as follows:

– With decreasing (increasing) metallicity the temperature in the disk drops (increases) as a consequence of an overall reduced (increased) opacity which is determined by dust and ice for temperatures lower than the dust sublimation temperature (∼1800 K). The dust-to-gas ratio is reduced to the same extent as the metallicity decreases.
– As the disks become cooler with decreasing metallicity they show a quasi-homologous inward shift of their temperature and density structures at a given instant. As a consequence, species such as crystalline forsterite, crystalline enstatite and solid carbon are less abundant in the outer disk regions in low metallicity models as compared to the solar abundance model. The strength of viscous accretion, however, is independent of metallicity in our one-zone model since we apply the β-viscosity which only depends on the radial coordinate. In the present model it is assumed that the turbulence in the disk also drives the radial mixing. For this reason the efficiency of mixing does not change with decreasing metallicity, i.e. decreasing opacity and temperature.
– The composition of the silicates strongly depends on the ratio of the abundances of Mg to Si, since in equilibrium between forsterite and enstatite Mg and Si both are completely condensed into a mixture of forsterite and enstatite. In case of $\epsilon_{\rm Mg}/\epsilon_{\rm Si} \sim 1$ enstatite grains are more abundant than forsterite grains by more than about an order of magnitude. At $\epsilon_{\rm Mg}/\epsilon_{\rm Si} = 1.5$ enstatite and forsterite have equal abundances. In case of $\epsilon_{\rm Mg}/\epsilon_{\rm Si} \geq 2$ enstatite is not stable under the conditions of protoplanetary disks, and forsterite is the only silicate existing in this case (with MgO bearing the excess Mg). However, the latter cases will rarely be realized in disks in the solar neighbourhood since in the most extreme cases [Mg/Si] is about $10^{0.3}$ in stars observed in the solar vicinity (Timmes et al. 1995; Ferrarotti & Gail 2001).
– As the Fe abundance decreases relative to the abundance of the silicate forming elements O, Mg and Si with decreasing metallicity, the relative abundance of solid iron drops in the low metallicity models.
– The abundance of ice (i.e. ice mantled grains) grows with increasing O abundance. The ice opacity feature therefore is more pronounced in models with enlarged O abundance.
– Corundum, which is considered in the model calculations as a representative for the most refractory solids in

protoplanetary disks, decreases in abundance as the Al abundance decreases. In typical solar neighbourhood stars with low metallicity ([Fe/H] $\lesssim -1.5$) Al is distinctly depleted relative to other key dust forming elements. This, and the fact that low metallicity models never experience temperatures as large as ∼1450 K above which corundum dominates the opacity of the disk until it disappears, makes corundum less important in low metallicity models of protoplanetary disks. This also holds for other refractory solids not considered in the present work, e.g. TiO and Al-Ca-Mg compounds such as diopside ($CaMgSi_2O_6$) and spinell ($MgAl_2O_4$).

– Carbon grains survive up to higher temperatures in models of low metallicity since the abundance of O and, thus, the concentration of OH decreases with decreasing metallicity, so that the carbon grains are oxidized less efficiently.
– The sun is an untypical star in its galactic environment with respect to the abundances of O, Mg, Si and Al. As a particular consequence the ratio of abundances of crystalline enstatite to crystalline forsterite (more general: crystalline pyroxene to crystalline olivine) in the solar nebula is higher-than-average as compared to protoplanetary disks with solar metallicity and a *typical* element mixture as for stars in the galactic vicinity of the sun.
– In β-disk models in the one zone approximation the evolution of the surface density Σ decouples from the thermal structure of the disk. Thus, the radial profiles of Σ in models of different metallicity at the same instant are the same. This is not the case for α-disk models. However, since we consider the vertical selfgravity of the disk in the model calculations, the α-prescription no more makes sense (Duschl et al. 2000). The mass density in β-disk models, in contrast, is still coupled to the thermal structure of the disk.
– The vertical selfgravitation of the disk leads to a large "gap" in the radial profile of the aspect ratio h_s/r in the intermediate and outer parts of the disk. This might lead to shadowing effects within the gap zone, i.e. the heating of the disk by irradiation of the star could be strongly reduced at the location of the gap. Irradiation of the upper layers of the disk by the star is not included in the present model calculations. This will be an issue of future investigations.

8. Conclusions

The main topic of this paper was to simulate protoplanetary accretion disks with element mixtures different from that of the solar system. In this context the composition of the primitive material from which larger bodies (asteroids, comets, planets) are built within protoplanetary disks is of particular interest for understanding the formation of planetary systems. In Paper IV and in the present work it has been shown that in the inner warm parts of the disk the original unequilibrated ISM dust transforms into thermally equilibrated dust. With respect to the silicate dust this equilibration process produces both crystalline enstatite and crystalline forsterite, respectively, whereby the ratio of the degrees of condensation of these species, $f_{\rm ens}/f_{\rm for}$, depends on the abundance ratio of Mg to Si.

However, observations of crystalline silicates in YSOs are rare. The only two certain detections of crystalline silicates in YSOs are TW Hya (Weinberger et al. 2002) and Hen 3–600 A (Honda et al. 2003), but only the latter authors fit the mid-IR spectrum of the disk by assuming a composition of both amorphous and crystalline silicates, and found a large fraction of about 50% crystalline silicates with $f_{\rm ens}/f_{\rm for} = 2/3$. This value of $f_{\rm ens}/f_{\rm for}$ is very low compared to the values resulting from the present model calculations of stars in the solar neighbourhood with typical element mixtures and indicates an unusually large Mg abundance or low Si abundance. Whether the crystalline silicates seen in these rather old disks actually originate from an annealing process, or if it is only exposed material which has formerly been processed within large protoplanetary bodies, remains open.

The value of $f_{\rm ens}/f_{\rm for}$ in the solar nebula, however, is not well known since primordial dust which condensates directly from the gas phase is hardly detected. Bradley et al. (1992) have analyzed the structure and composition of a sample of interplanetary dust particles (IDPs) and found two IDPs to resemble the infrared spectrum around the 10 μm silicate feature of the comets P/Halley (1986 03) and Bradfield (1987 29). Moreover, these IDPs show no indication of aqueous alteration, which points to the condensation of these small crystalline silicate grains ($\lesssim$100 nm) within their glassy matrix from nebula gas without being processed within large bodies afterwards. The ratio between Fe poor pyroxenes and olivines in these IDPs found by Bradley et al. (1992) is roughly 2:1. This is rather low compared to $f_{\rm ens}/f_{\rm for} \sim 12$ expected for the solar nebula and indicates a rather large $\epsilon_{\rm Mg}/\epsilon_{\rm Si}$ of about 4/3 (standard solar value: ∼1.08) or the accumulation of either IDP material within a relatively narrow zone of around 1280 K in the disk where enstatite transforms into forsterite (at around 0.5 AU after 10^5 yr; see Figs. 6 and 10a) which seems unlikely, however.

In contrast to the low value of $f_{\rm ens}/f_{\rm for}$ in IDPs found by Bradley et al. (1992), Wooden et al. (1999) found a crystalline pyroxene-to-olivine ratio in comet Hale-Bopp of $9.0^{+7.2}_{-3.5}$ (1σ confidence) by fitting IR spectra of the comet at different heliocentric distances. In a further analysis Wooden et al. (2000) fit the IR spectra of Hale-Bopp by spectra of single IDPs which show extreme pyroxene and olivine contents, respectively, and found crystalline pyroxene-to-olivine ratios in the range 3.5 . . . 8. These results are more consistent with the value of $f_{\rm ens}/f_{\rm for} = 12$ at the birth place of the comets calculated in the present model with solar abundance. Moreover, Wooden et al. (1999) found the spectra of Hale-Bopp best matched by silicates with Mg numbers Mg/(Mg + Fe) ∼ 0.9, i.e. with respect to its composition the crystalline pyroxene (olivine) in comet Hale-Bopp is almost pure enstatite (forsterite). As well Bradley (1999) found Mg numbers of >0.9 in a sample of crystalline pyroxene and olivine grains extracted from polar micrometeorites and IDPs for almost the entire sample. A possible explanation for the observed large Mg numbers in these likely pristine silicate grains of the solar nebula is that the unequilibrated (amorphous) ISM pyroxene and olivine grains entering the solar nebula were subject to an annealing/equilibration process within the solar nebula which transforms them into crystalline enstatite and olivine grains.

Finally we like to remark that the metallicity increases towards the galactic center as the synthesis of heavy elements proceeds more rapid in the inner as compared to the outer parts of the galactic disk. Actually, Laws et al. (2003) found in their statistical analysis the frequency of planetary system, respectively planets, to increase towards the galactic center.

We conclude with the remark that the present work serves as a further building block within this series that attempts to explain the composition of planetary system bodies, especially the composition of asteroids and comets of the solar system.

Acknowledgements. This work is supported by the Deutsche Forschungsgemeinschaft (DFG), Sonderforschungsbereich 359 "Reaktive Strömungen, Diffusion und Transport", and by a Ph.D. grant of the Landesgraduiertenförderung Baden Württemberg.

Appendix A: Inner boundary condition

Previous calculations of disk evolution in the one-zone approximation (e.g. Lin & Papaloizou 1985; Ruden & Lin 1986; Ruden & Pollack 1991; Bell & Lin 1994) show that the innermost disk region rapidly develops on the short viscous timescale of the innermost disk region into a quasi-stationary state where the mass accretion rate $\dot{M}$ is radially nearly constant over an extended region in the inner parts of the disk. The value of $\dot{M}$ in this region gradually changes in time, however. This suggests that it is possible to calculate the disk structure in the innermost parts of the disk as for a stationary disk.

In this case, the structure of the stationary inner disk is determined by $\dot{M}$ (and the stellar mass M_*), which are free parameters within the frame of the theory of stationary one-zone disk models. These free parameters have to be determined by coupling the stationary inner disk evolution to the time dependent calculation of the disk evolution in the outer parts at some radius r_1. This radius r_1 serves as the inner boundary for the outer time dependent model and as the outer radius for the quasi-stationary inner disk.

The difference equation for $\dot{M}$ at the inner boundary of the time dependent model is (cf. Eq. (31) in Paper II)

$$\dot{M}_1 = -\frac{3\pi}{\sqrt{r_2}-\sqrt{r_1}}\left(\nu_2\Sigma_2\sqrt{r_2}-\nu_1\Sigma_1\sqrt{r_1}\right), \tag{A.1}$$

where ν_2 and Σ_2 are the viscosity and surface density at the second innermost grid point of the time dependent model. They are to be calculated from the solution of the equations for the time dependent radial disk structure. However, ν_1 and Σ_1 are not known in advance. They have to be calculated from the set of equations for the disk structure at $k = 1$ in the *stationary* case. The basic set of equations in this case is formed by Eqs. (22)–(32) and

$$\Sigma_1 = \frac{|\dot{M}_1|}{3\pi\nu_1}\left(1-\sqrt{\frac{R_*}{r_1}}\right), \tag{A.2}$$

which replaces Eq. (21). These equations can be solved, if ν_2 and Σ_2 are prescribed. These equations form a nonlinear set of equations for the basic disk quantities of the disk, including $\dot{M}_1$. As a result one obtains $\dot{M}_1$ as a function of the assumed values of ν_2 and Σ_2. Since ν_2 itself is a function of Σ_2, one basically obtains a relation

$$\Sigma_1^{(m)} = \Psi(\Sigma_2^{(m)}), \tag{A.3}$$

where the function Ψ is determined by the solution of the set of Eqs. (A.1), (22)–(32) and (A.2).

To connect the structure of the stationary inner disk with the structure of the time dependent outer disk we proceed as follows: let m denote the current iteration step of the global iteration of the surface density Σ (see Fig. 1). The solution for Σ_1 within the global iteration is

$$\begin{aligned}\Sigma_1^{(m)}+\delta\Sigma_1 &= \Psi(\Sigma_2^{(m)}+\delta\Sigma_2)\\ &\approx \Psi(\Sigma_2^{(m)})+\left.\frac{\partial\Psi}{\partial\Sigma_2}\right|_{\Sigma_2^{(m)}}\delta\Sigma_2,\end{aligned} \tag{A.4}$$

where we terminate the expansion of Ψ after the linear term. $\delta\Sigma_1$ and $\delta\Sigma_2$ are the corrections of $\Sigma_1^{(m)}$ and $\Sigma_2^{(m)}$ in the mth global iteration step. From Eq. (A.4) the correction $\delta\Sigma_1$ is approximately given by

$$\delta\Sigma_1 \approx \left.\frac{\partial\Psi}{\partial\Sigma_2}\right|_{\Sigma_2^{(m)}}\delta\Sigma_2. \tag{A.5}$$

We substitute Eq. (A.5) by a difference scheme,

$$\delta\Sigma_1 \approx \frac{\Psi(\Sigma_2)-\Psi(\Sigma_2')}{\Sigma_2-\Sigma_2'}\,\delta\Sigma_2, \tag{A.6}$$

with $\Sigma_2' = (1-10^{-6})\Sigma_2$. The values of $\Sigma_2^{(m)}$ and $\delta\Sigma_2$, respectively, are given from the solution of the set of Eqs. (21)–(32) for the time dependent outer disk structure since the set of Eqs. (21)–(32) is solved at each radial point k by starting at the outer boundary $k = K$ and then by moving radially inwards through the set of grid-points down to the second innermost point $k = 2$. Also the value of ν_2 is given from the solution of the set of Eqs. (21)–(32).

Given these values of ν_2 and Σ_2 the set of equations. for the structure of the *stationary* inner disk is solved twice (for Σ_2 and Σ_2') with a Newton-Raphson method up to an accuracy of 10^{-6}. From Eq. (A.6) the correction $\delta\Sigma_1$ to Σ_1 is obtained. The global solution for the time dependent disk structure is obtained by globally iterating Σ up to an accuracy of 10^{-5} (see Fig. 1).

The quasistationary inner boundary condition omits the unphysical descent of the surface density and of other relevant quantities such as the temperature at the inner disk edge which results from the no-torque inner boundary condition ($\Sigma_1 = 0$). A further advantage of the quasistationary inner boundary condition is that it comprises no restriction for the choice of the location of the inner boundary r_1, i.e. r_1 within a disk model can be chosen far outwards without the risk of unphysical deviations from the real disk structure. The only restriction is that one has to be sure that the disk is quasistationary inside of r_1. The quasistationary inner boundary condition can not be applied, however, to time dependent phenomenons such as the FU Orionis outbursts which are attributed to a thermal instability in the inner parts of protoplanetary disks (Hartmann & Kenyon 1996). In this case the mass accretion rate at the inner

edge $\dot{M}_1$ is a strongly time dependent quantity, and therefore a different suitable inner boundary condition has to be applied in this and other such cases.

References

Allende Prieto, C., Lambert, D. L., & Asplund, M. 2002, ApJ, 573, L137
Anders, E., & Grevesse, N. 1989, Geochim. Cosmochim. Acta, 53, 197
Bell, K. R., & Lin, D. N. C. 1994, ApJ, 427, 987
Boss, A. P. 2000, ApJ, 536, L101
Bradley, J. P., Humecki, H. J., & Germani, M. S. 1992, ApJ, 394, 643
Bradley, J. P., Snow, T. P., Brownlee, D. E., et al. 1999, in Solid Interstellar Matter: The ISO Revolution, ed. L. d'Hendecourt, C. Joblin, & A. Jones (Springer-Verlag and EDP Sciences), 297
Demyk, K., Carrez, Ph., Leroux, H., et al. 2001, A&A, 368, L38
Draine, B. T. 1985, ApJS, 57, 587
Duschl, W. J., Gail, H.-P., & Tscharnuter, W. M. 1996, A&A, 312, 624
Duschl, W. J., Mayer, M. 2003, in preparation
Duschl, W. J., Strittmatter, P. A., & Biermann, P. L. 2000, A&A, 357, 1123
Fabian, D., Jäger, C., Henning, Th., et al. 2000, A&A, 364, 282
Ferrarotti, A. S., & Gail, H.-P. 2001, A&A, 371, 133
Finocchi, F., Gail, H.-P., & Duschl, W. J. 1997, A&A, 325, 1264
Gail, H.-P. 2001, A&A, 378, 192
Gail, H.-P. 2002, A&A, 390, 253
Gail, H.-P. 2003, A&A, submitted
Haisch Jr., K. E., Lada, E. A., & Lada, C. J. 2001, ApJ, 553, L153
Hanner, M. S., Lynch, D. K., & Russel, R. W. 1994, ApJ, 425, 274
Harker, D. E., Wooden, D. H., Woodward, C. E., et al. 2002, ApJ, 580, 579
Hartmann, L., & Kenyon, S. J. 1996, ARA&A, 34, 207
Hayashi, C. 1981, Prog. Theor. Phys. Suppl., 70, 35
Hirschfelder, J. O., Curtiss, C. F., & Bird, R. B. 1964, Molecular Theory of Gases and Liquids (New York: Wiley)
Honda, M., Kataza, H., Okamoto, Y. K., et al. 2003, ApJ, 585, L59
Huré, J.-M. 2000, A&A, 358, 378
Huré, J.-M., Richard, D., & Zahn, J.-P. 2001, A&A, 367, 1087
Keeley, D. A. 1970, ApJ, 161, 643
Koike, C., Kaito, C., Yamamoto, T., et al. 1995, Icarus, 114, 203
Laws, C., Gonzalez, G., Walker, K. M., et al. 2003, AJ, 125, 2664
Lide, D. R. 1995, CRC Handbook of Chemistry and Physics, 78th ed. (CRC Press, Boca Raton etc.)
Lin, D. N. C., & Papaloizou, J. 1985, in Protostars & Planets II, ed. D. C. Black, & M. S. Matthews (Tucson: University of Arizona Press)
Lissauer, J. J. 1987, Icarus, 69, 249
Marigo, P. 2002, A&A, 387, 507
Mathis, J. S., Rumpl, W., & Nordsieck, K. H. 1977, ApJ, 217, 425
Nakamoto, T., & Nakagawa, Y. 1994, ApJ, 421, 640
Nakamoto, T., & Nakagawa, Y. 1994, ApJ, 445, 330
Natta, A. 1999, in Infrared Space Astronomy, To-day and To-morrow, ed. F. Casoli, F. David, & J. Lequeux (Springer Verlag), 1
Paczyński, B. 1978, Acta Astron., 28, 91
Philpotts, A. R. 1990, Principles of igneous and metamorphic petrology (Prentice Hall, Englewood Cliffs, New Jersey)
Pollack, J. B., Hollenbach, D., Beckwith, S., et al. 1994, ApJ, 421, 615
Pollack, J. B., Hubickyj, O., Bodenheimer, P., et al. 1996, Icarus, 124, 62
Portinari, L., Chiosi, C., & Bressan, A. 1998, A&A, 334, 505
Richard, D., & Zahn, J.-P. 1999, A&A, 347, 734
Ruden, S. P., & Lin, D. N. C. 1986, ApJ, 308, 883
Ruden, S. P., & Pollack, J. B. 1991, ApJ, 375, 740
Santos, N. C., Israelian, G., Mayor, M., et al. 2003, A&A, 398, 363
Sharp, C. M., & Huebner, W. F. 1990, ApJS, 72, 417
Stepinski, T. F. 1998, ApJ, 507, 361
Taylor, G. I. 1936, Proc. R. Soc. London, 157, 546
Taylor, G. I. 1936, Proc. R. Soc. London, 157, 565
Thommes, E. W., Duncan, M. J., & Levison, H. F. 2003, Icarus, 161, 431
Timmes, F. X., Woosley, S. E., & Weaver, T. A. 1995, ApJS, 98, 617
Toomre, A. 1964, ApJ, 139, 1217
Wehrstedt, M., & Gail, H.-P. 2002, A&A, 385, 181
Weidenschilling, S. J., & Cuzzi, J. N. 1993, in Protostars & Planets III, ed. E. H. Levy, & J. I. Lunine (Tucson: University of Arizona Press), 1031
Weinberger, A. J., Becklin, E. E., Schneider, G., et al. 2002, ApJ, 566, 409
Wendt, F. 1933, Ingenieur-Archiv IV, 577
Wetherill, G. W. 1989, in Asteroids II, ed. R. P. Binzel, T. Gehrels, & M. S. Matthews (Tuscon: Univ. of Arizona Press), 661
Wooden, D. H., Harker, D. E., Woodward, C. E., et al. 1999, ApJ, 517, 1034
Wooden, D. H., Butner, H. M., Harker, D. E., et al. 2000, Icarus, 143, 126